DISSERTATION

DOSIMETRY AND CLUSTERING PROPERTIES OF ENERGY DEPOSITION FROM BETA PARTICLES EMITTED BY H-3 AND C-14 IN THE NUCLEUS OF A MAMMALIAN CELL

Submitted by

Vladimir Semenenko

Department of Environmental and Radiological Health Sciences

In partial fulfillment of the requirements

For the Degree of Doctor of Philosophy

Colorado State University

Fort Collins, Colorado

Spring 2003

ProQuest Information and Learning Company
300 North Zeeb Road
P.O. Box 1346
Ann Arbor, MI 48106-1346

COLORADO STATE UNIVERSITY

January 16, 2003

WE HEREBY RECOMMEND THAT THE DISSERTATION PREPARED UNDER OUR SUPERVISION BY VLADIMIR SEMENENKO ENTITLED DOSIMETRY AND CLUSTERING PROPERTIES OF ENERGY DEPOSITION FROM BETA PARTICLES EMITTED BY H-3 AND C-14 IN THE NUCLEUS OF A MAMMALIAN CELL BE ACCEPTED AS FULFILLING IN PART REQUIREMENTS FOR THE DEGREE OF DOCTOR OF PHILOSOPHY.

Committee on Graduate Work

Martin P. Gelfand

Robert L. Ullrich

Joel S. Bedford

Adviser — Thomas B. Borak

Department Head — F. Ward Whicker

ABSTRACT OF DISSERTATION

DOSIMETRY AND CLUSTERING PROPERTIES OF ENERGY DEPOSITION FROM BETA PARTICLES EMITTED BY H-3 AND C-14 IN THE NUCLEUS OF A MAMMALIAN CELL

It has been suggested that the more densely ionizing terminal portion of an electron track could be responsible for the majority of biological damage as opposed to the less densely ionizing initial part of the track. To test this hypothesis, it is proposed to compare chromosome aberration yields when cell nuclei are irradiated by incorporated ^{3}H and ^{14}C. The rationale is that virtually all electron tracks from ^{3}H would originate and terminate in the nucleus, whereas almost none of the β particles would stop inside the nucleus for ^{14}C. Since the intention would be to determine RBE values, careful evaluation of dosimetry of β particles from decays of ^{3}H and ^{14}C in the nucleus of a cell is necessary. Three aspects of this dosimetry were addressed: 1) the intranuclear dose, 2) the internuclear dose, and 3) the fraction of dose deposited by electron track ends. A Monte Carlo electron track-structure code was used as the primary tool for solving these problems. Comparisons of results produced by three different Monte Carlo codes in terms of energy deposition in spherical volumes showed good agreement. Track-structure codes were also compared with other analytical methods for beta dosimetry reported in the literature. The intranuclear dose from both radionuclides was calculated

for a variety of nuclear sizes under assumptions of spherical and ellipsoidal geometry for a cell nucleus. A method for estimating the internuclear dose for cells with nuclei of different geometries was described. For cells with flat nuclei, similar to those that will be used in the experiments, the internuclear dose was determined to be negligible for ^{3}H and a few percent of the intranuclear dose for ^{14}C. A *K*-means clustering algorithm was employed to characterize electron track ends. Criteria were developed and implemented in a scoring procedure to identify clusters associated with track ends of primary and secondary electrons and separate these from the less densely ionizing portion of electron tracks. The fraction of dose due to electron track ends was estimated as ~43% for ^{3}H and ~30% for ^{14}C. These values were independent of geometry for a cell nucleus.

Vladimir Semenenko
Department of Environmental and
Radiological Health Sciences
Colorado State University
Fort Collins, CO 80523
Spring 2003

ACKNOWLEDGMENTS

This research was funded by grant CA80651 from the National Cancer Institute, National Institutes of Health.

I also would like to thank the following people:

- My advisor, Dr. Thomas B. Borak, for his overwhelming support and participation throughout my research.
- Dr. Joel S. Bedford and his graduate student Paul Wilson in the Department of Environmental and Radiological Health Sciences at Colorado State University for their work on the biological portion of this project. I am also indebted to Dr. Bedford for the financial support.
- Committee members for taking time out of their busy schedules.
- Drs. Bulent Aydogan and Wesley E. Bolch at University of Florida, FL for providing samples of electron tracks generated with the Monte Carlo code OREC, which allowed me to get started with this project.
- Dr. James E. Turner in Oak Ridge, TN for generously granting an unlimited access to the Monte Carlo code NOREC. This work would not have been completed within the same timeframe otherwise. It was a great honor to work with Dr. Turner on improving the code.

- Dr. Hooshang Nikjoo at MRC Radiation and Genome Stability Unit, Harwell, Oxfordshire,UK for providing electron histories generated with the code KURBUC for comparisons.
- Drs. Werner Friedland and Herwig G. Paretzke at GSF – National Research Center for Environment and Health, Neuherberg, Germany for providing electron tracks generated with the Monte Carlo code PARTRAC.
- Dr. Roger W. Howell at New Jersey Medical School, NJ for helpful discussions about cellular dosimetry.
- Staff in the Department of Environmental and Radiological Health Sciences at Colorado State University: Julie Asmus, Sandy Wiggen and Norma Bulera.

TABLE OF CONTENTS

LIST OF TABLES

LIST OF FIGURES

CHAPTER 1. INTRODUCTION

Ultrasoft X-ray studies

There has been a large effort by different research groups to determine relative biological effectiveness (RBE) of ultrasoft X rays (X rays with energies <5 keV, of which the most commonly encountered are C_K (0.28 keV), Cu_L (0.96 keV), Al_K (1.5 keV) and Ti_K (4.5 keV) X rays). An overwhelming majority of such studies, conducted in a wide variety of biological systems using various endpoints, report RBEs appreciably greater than one (*1-9*). Ultrasoft X rays interact with biological material predominantly by photoelectric effect producing low-energy electrons that resemble the terminal part of higher energy electron tracks. It was suggested that such "track ends", characterized by high density of energy deposition, possess greater ability to produce critical biological damage than the sparsely ionizing component of an electron track (*8-11*).

The dosimetry of ultrasoft X rays presents difficulties due to their severe attenuation even when penetrating a cell nucleus. The attenuation length in water of Al_K X rays is about 7 μm and that of C_K X rays is only ~2 μm (*4*). As a result, there is a gradient of dose through a cell nucleus. Typically, mean nuclear doses in the above-mentioned experiments were calculated based on measurements of entrance doses and nuclear thickness.

There are also a few reports of the RBE for ultrasoft X rays being near unity (*12-14*). There authors had used cells with very flat nuclei, which greatly diminished

variations of the absorbed dose along the short axis of a nucleus. High RBE values found in previous studies were thus attributed to the use of mean dose, which might not be an appropriate descriptor when there is a highly uneven dose distribution in a cell nucleus. If this were the case, it would argue against the hypothesis that the majority of biological damage that follows exposure to low-LET radiations results from low-energy, track-end electrons.

Proposed experiment

To further test the hypothesis, it was proposed to compare chromosome aberration induction per unit nuclear dose following uniform incorporation of ^{3}H and ^{14}C into cell nuclei of a monolayer culture (Fig. 1). Table 1 summarizes the properties of the two β-particle-emitting radionuclides.

Table 1. Properties of ^{3}H and ^{14}C.

	^{3}H	^{14}C
Half-life, years	12.3	5730
Average energy, keV	5.7	49
Maximum energy, keV	18.6	156
Average range in water, μm	~1	~40
Maximum range in water, μm	~8	~300

Since the dimensions of a cell nucleus are of the order of 5 to 10 micrometers, the rationale is that most tritium β particles will originate and terminate within the nucleus. Thus, these electrons will deposit their entire energy, including track ends, inside the nucleus. Since β particles from ^{14}C have much larger energies, they will originate within

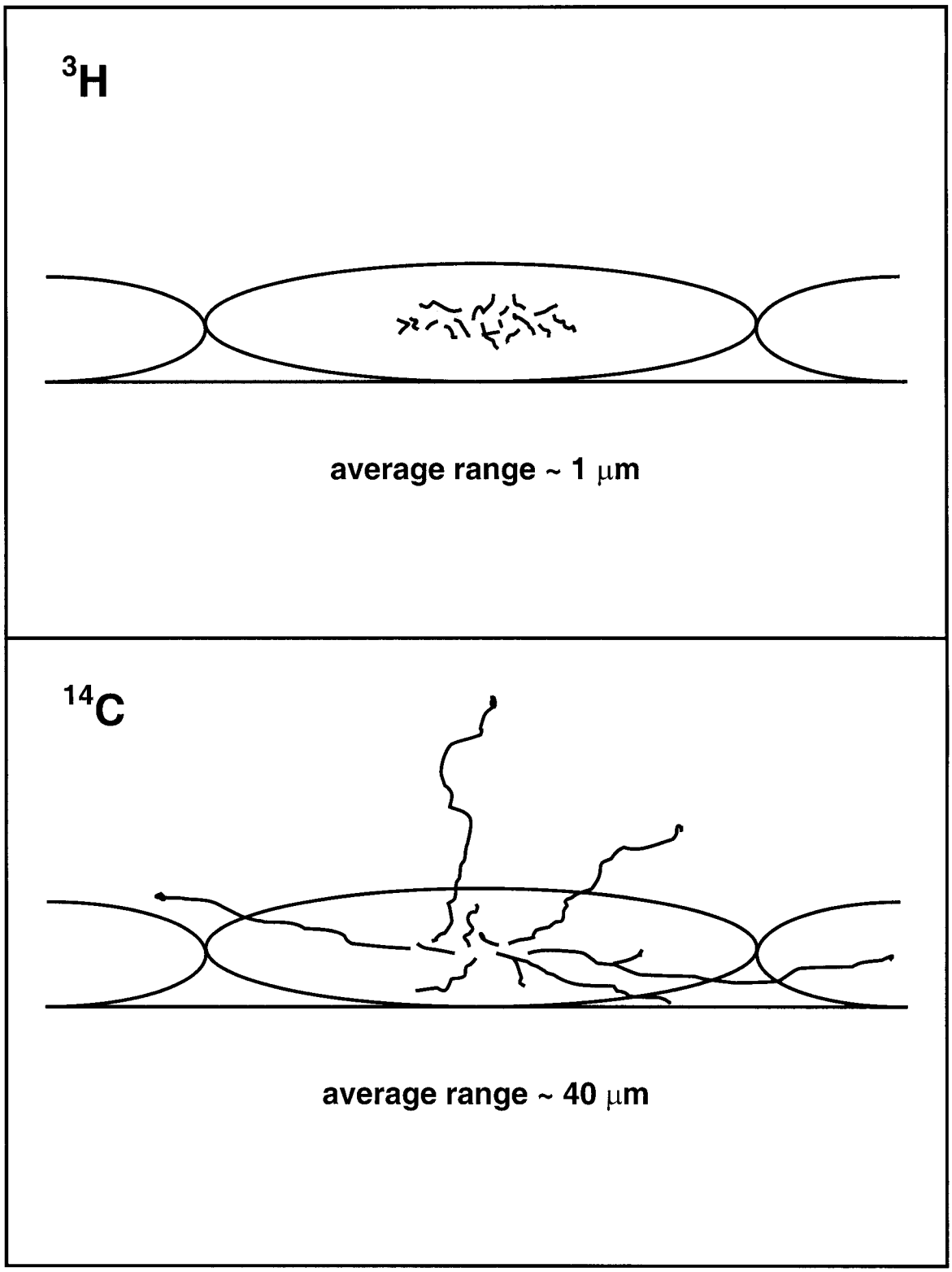

Figure 1. Chromosome-aberration experiments with ^{3}H and ^{14}C. β particles originate in the nucleus (gray area). NOTE: Not to scale.

the nucleus but terminate outside of the nucleus in most cases. This means that for ^{3}H, nuclear dose would be deposited predominantly as a highly clustered, "high-LET" portion of electron tracks. On the other hand, β particles from ^{14}C would deposit their dose in the form of high-energy, "low-LET" portion.

These statements are valid providing that 1) nuclei receive a small amount of energy deposition from track ends of secondary electrons; 2) contribution from electrons originating in nuclei of neighboring cells and depositing their track ends in a target cell is also small. Secondary and higher order electrons are created in abundance as the primary electron penetrates through matter. Each of such electrons deposits its energy in a pattern similar to that of a primary electron with the same energy. Some energetic enough secondary electrons can therefore form energy deposition patterns analogous to those from electron track ends. The dose contribution from neighboring cells will be reduced for the case of monolayer culture of contact-inhibited cells. As opposed to three dimensional situation, such as might be the case for cells in tissue, in the case of a monolayer culture, a target nucleus will subtend a very small solid angle from neighboring cells' nuclei, which should minimize its chances of being crossed by tracks of β particles originating in those nuclei. These assumptions are of more concern for ^{14}C, because its β particles have longer ranges and are capable of producing more energetic secondary electrons. If all these speculations are true, the increased yield of chromosome aberrations per unit absorbed dose is expected from incorporated ^{3}H compared to ^{14}C, which would supply further evidence in favor of the "track ends hypothesis".

In RBE studies of ultrasoft X rays, low-energy X rays, which produce a dose gradient through individual cells, were compared to reference radiation (usually hard X

rays), which produces uniform dose distribution. It was argued that observed high RBEs could be an artifact of such comparisons. In the proposed radiobiological experiments, uniform irradiation of cell nuclei with both ^{3}H and ^{14}C will be achieved providing that DNA is labeled homogeneously. Because chromosome aberration yields per unit dose are to be compared and RBE values for ^{3}H and ^{14}C are to be determined, it is important to know exact absorbed doses received by cell nuclei in both cases. For this reason, the dosimetry of β particles from the decay of ^{3}H and ^{14}C incorporated into a cell nucleus was elevated to a separate project and became the subject of this dissertation.

The objective of this work is therefore threefold:

1) to calculate intranuclear dose due to β particles from the decay of ^{3}H and ^{14}C uniformly incorporated into the nucleus of a cell;

2) to characterize track-end clusters of energy deposition events by electrons and estimate the fraction of such events in parts of ^{3}H and ^{14}C spectra deposited in a cell nucleus;

3) to estimate internuclear dose deposited by β particles originating in nuclei of neighboring cells and its significance in terms of additional track-end energy depositions.

It should be noted that, since direct measurements are not feasible for the problems of interest, any dosimetric estimates would have to be obtained by means of analytical calculations or modeling.

CHAPTER 2. REVIEW OF LITERATURE

Intranuclear dose

The mean dose absorbed in a volume homogeneously labeled with a beta emitter can be calculated according to the formula (*15*):

$$D[rad] = 3.56 \cdot 10^{-2} A \cdot \overline{E}_{\beta} \cdot t \ , \qquad (1)$$

where t is the time in minutes;

$\overline{E}_{\beta}$ is the average beta energy in MeV;

A is the specific activity in μCi/g.

This formula assumes that $t << T_{1/2}$, radionuclide's half-life, and is valid for time constant specific activity.

If dimensions of the volume are significantly larger than ranges of β particles, dosimetry based on the average energy, such as in equation 1, is a satisfactory approximation. However, this condition is not met for ^{3}H and ^{14}C uniformly distributed in the nucleus of a cell. The dimensions of an average cell nucleus are of the same order of magnitude as CSDA ranges of β particles in case of ^{3}H and considerably less than those for ^{14}C. Thus the average energy absorbed in a nucleus, $\overline{E}_{abs}$, comprises only a portion of the emitted energy, $\overline{E}_{\beta}$. Equation 1 should then be modified by replacing $\overline{E}_{\beta}$

with $\overline{E}_{abs}$. It is an essential task of beta dosimetry to determine the average absorbed energy, which is dependent upon the energy spectrum of a beta-emitting radionuclide and the dimensions of a target.

The great deal of work on the dosimetry of ^{3}H and ^{14}C incorporated into a cell nucleus was accomplished in 1960s and early 1970s when these radionuclides, especially tritium, were extensively used in radiobiological studies. The comprehensive summary of the early work can be found in (*15, 16*).

Due to the nature of the problem (low energy of emitted β particles and small-sized targets) the direct experimental approach was not suitable. For that reason, the dosimetry of ^{3}H and ^{14}C was accomplished by means of theoretical calculations. Such calculations often involved integrations over the volume of a cell nucleus. The integrations had to be made analytically, as numerical approaches were limited by the development of computers at the time. As a result, the most probable case of ellipsoidal geometry for a nucleus was substituted by the assumption of the spherical nucleus, which was easier to handle due to its symmetry. The problem of dosimetry for elliptical nuclei is briefly addressed in (*15*). The authors describe a very crude approach to estimation of absorbed dose, which is not suitable for elongated ellipsoids. In a more recent work related to the dosimetry of Auger-electron emitters for ellipsoidal geometry, a numerical method is presented for prolate spheroids (*17*).

Historically, the majority of methods in beta dosimetry, including the dosimetry of beta emitters incorporated into a cell nucleus, were based on point kernels or point-source functions (*16, 18-29*). These describe the distribution of absorbed dose around an isotropic source of β particles. The point-kernel method is suitable for sources uniformly

distributed in homogeneous medium. It involves two steps: determining the point kernel, either experimentally when possible, or from theoretical considerations, and integrating the point kernel over the volume of interest to obtain total absorbed dose.

One of the first point-source functions had the form (*18, 19*)

$$D(r) = \frac{\overline{E}_\beta \mu}{4\pi} \cdot \frac{e^{-\mu r}}{r^2} \tag{2}$$

Here $\overline{E}_\beta$ is the average beta energy, μ is an empirical absorption coefficient, and r is the distance from the point source. Equation 2 is similar to the point kernel used routinely in photon dosimetry. In this way, information accumulated for extended photon sources of different geometries can be applied directly to problems of beta dosimetry. While this approach worked for more energetic beta emitters, Robertson *et al.* pointed out (*23*) that equation 2 could not satisfactory fit the results of their theoretical calculations for tritium (*21, 22*). A falloff of dose for tritium was too slow to be adequately described by an equation with the $1/r^2$ component. This is generally attributed to low energies of tritium β particles and, to the less extent, applies to ^{14}C as well. As a result, many works on the dosimetry of ^{14}C, and especially ^{3}H, use unconventional forms of a point kernel.

Loevinger (*20*) used measurements on a wide range of point β-particle sources in air to derive the empirical formula for the point kernel:

$$\left.\begin{array}{c} r^2 I = k\{[c - re^{1-(r/c)}]_1 + [re^{1-r}]_2\} \\ [\ ]_1 \equiv 0,\ r \geq c \end{array}\right\}, \tag{3}$$

where I is the point-source distribution function, that is, the absorbed energy per gram per disintegration at a distance $r = \mu x$ from a point source of β particles;

$k = \dfrac{\mu^3 \overline{E} \rho_m^2}{400\pi[c^2(3-e)+e]} rad$ is a normalization constant;

μ is a parameter (in cm^2/g) identified as the apparent absorption coefficient;

$\overline{E}$ is the average β-particle energy per disintegration in ergs;

ρ_m is the density of the absorbing material in g/cm^3;

c is a dimensionless model parameter;

e is the base of natural logarithm.

Loevinger also analyzed data derived from measurements on plane β-particle sources in polystyrene. Based on these considerations, he recommended the following values of the parameters for soft tissue (*20, 27*):

$$c = \begin{cases} 2 & 0.17 < E_0 < 0.5\,MeV \\ 1.5 & 0.5 < E_0 < 1.5\,MeV \\ 1 & 1.5 < E_0 < 3\,MeV \end{cases}$$

$$\mu = \frac{18.6}{(E_0 - 0.036)^{1.37}} \left(2 - \frac{\overline{E}}{\overline{E}^*}\right) \text{cm}^2/\text{g of tissue}, \qquad (4)$$

where E_0 is the maximum energy of the β-particle spectrum in MeV and $\overline{E}^*$ is the average energy per disintegration for a hypothetical allowed spectrum of the same maximum energy.

Robertson and Hughes have described a method to calculate the point kernel for tritium based on the knowledge of its β spectrum, ranges and rate of energy loss for electrons (*21, 22*). The following fit to the calculated data was provided (*23*):

$$D(r) = 185e^{-5.55r} + 15e^{-1.92r} , \tag{5}$$

where D is the average dose per disintegration in rads and r is the distance from a point source in microns.

Goodheart (*24*) has also published a fit to the data of Robertson and Hughes claiming it is easier to integrate (D is in rads and r is in μm):

$$D(r) = \frac{3}{(0.01 + r^2)(1 + 0.1r^2)(1 + 0.2r^2)} \tag{6}$$

Stewart (*25*) has suggested a fit to the curve obtained by Robertson and Hughes in the form of equation 2 with $1/\mu = 1.5$ microns.

Künkel (*26*) has used the method similar to that of Robertson and Hughes to calculate the point kernel for tritium. No fit to the data was supplied.

Berger (*28*) has tabulated percentile distances, x_p, in water (distance from a point source within which p% (p = 5, 10, ..., 95) of the source energy is deposited) for 75 beta-emitting radionuclides including those two of interest. The point kernels for ^3H and ^{14}C can be derived from these data. The percentile distances for tritium are based entirely on

an extrapolation from the energy region above 25 keV, and therefore these data should be used with extreme caution.

To calculate point-source function for tritium, Shiragai (*16*) has employed the method he called "constant absorption model", which is not conceptually different from previously described methods (*22, 26*). In a successive publication (*29*), Shiragai has applied the energy dissipation model by Kobetich and Katz (*30*) to the problem. Although no fits to the point kernels obtained by the two methods were given, Shiragai provides valuable comparisons of his calculations with the previous results of Robertson and Hughes (*22, 23*) and Künkel (*26*).

Once the expression for a point kernel is found, the next step in calculating the total absorbed dose to a cell nucleus is to integrate the point kernel over the volume of a nucleus. This can be achieved either by a two-step integration as described in (*15*) or with the use of geometrical reduction factors (*27, 31*). The results of such integrations for the two forms of a point kernel (eqs. 2 and 5) are presented in (*15*).

Methods for calculating dose to a cell nucleus from ^{3}H and ^{14}C other than the point-kernel method have also been reported. Apelgot and Duquesne (*32*) have estimated the average dose absorbed in a spherical nucleus of radius R due to uniformly incorporated tritium as

$$D = \left[1.77 + 0.25\left(\frac{R-1}{R}\right)^{3}\right] 10^{-2} \text{ ergs min}^{-1}\ \mu\text{Ci}^{-1}\ \mu\text{m}^{-3} \qquad (7)$$

The formula is valid for $R \geq 2$ μm.

Kühn (*33*) has calculated the average energy absorbed in a cell nucleus using the following equation:

$$\overline{E} = \sum_{i=1}^{l} W_i E_i + \overline{L} \sum_{i=l+1}^{n} W_i \left(dE/dx\right)_i \ , \qquad (8)$$

where W_i is the relative frequency of ith energy interval with the midpoint energy E_i in the β spectrum divided into n intervals. He has assumed that energy of β particles is completely absorbed in the sphere if their ranges less than a mean distance $\overline{L}$ between all the points inside the sphere and the surface of the sphere (first term in the formula). Kühn reports this distance to be equal $\overline{L} = 1.2R$ for a spherical nucleus of radius R. The contribution from the more penetrating portion of the β spectrum, which is only partially absorbed, is determined as the product of linear energy loss for a particular energy interval and the distance $\overline{L}$ (second term).

In summary, the majority of publications on the dosimetry of ^{3}H and ^{14}C homogeneously distributed in the nucleus of a cell employed the point-kernel method assuming a spherical geometry for a cell nucleus. Some of the most commonly used forms of a point kernel have been integrated over the volume of a sphere and these results are reported in the literature (*15*).

Fraction of dose deposited by low-energy electrons

In order to understand the increased effectiveness of ultrasoft X rays, several investigators have made estimates of the fraction of energy deposited by electrons similar

to those produced by ultrasoft X rays in case of different low-LET radiations. Raju *et al.* (*4*) report that nearly one-third of the energy of 250-kVp X rays is deposited by electrons with energies comparable to those from ultrasoft X rays. However, the authors do not reveal the origin of their estimate. Goodhead (*34*) has plotted cumulative fractions of dose from low-LET radiations deposited locally (energy deposition <100 eV is considered local) by electrons of different energies in the equilibrium slowing-down spectrum and concluded that for all low-LET radiations, low-energy electrons less than 5 keV contribute ~30-50% of the total absorbed dose. Later Nikjoo and Goodhead (*11*) have repeated this analysis with the use of a Monte Carlo electron-transport code. Their conclusion was that low-energy secondary electrons account for up to ~50% of the total dose imparted to a medium when irradiated with electrons or photons. In a more recent publication by Nikjoo *et al.* (*35*), it was claimed that, based on clustered-damage evaluation, ~30% of dose (radiation was not specified) is deposited by low-energy electrons. The authors also gave no details of the calculation.

The authors of several studies (*35-40*) applied clustering analysis to Monte Carlo calculations of track structure in attempts to find correlation between the occurrence of clusters of ionizations and biological damage (usually production of double-strand breaks) for different radiations. All the studies were focused on nanometer-sized clusters of just several ionizations. These events are clearly not comparable to track-end energy depositions considered in this research, because energy of electrons produced by different ultrasoft X rays ranges between several hundred eV and several keV. Such energy deposition events occur on a much larger spatial scale and contain tens to hundreds of interactions. Furthermore, we are interested in overall energy deposition by track-end

clusters without singling out ionizations. Although results of these studies cannot be related to the problem of interest, some ideas developed therein can be adopted in the current research.

Internuclear dose

We could find only one published report that addresses problem of dose from neighboring cells (*41*). The authors consider a wide variety of radiation sources: Auger-electron-emitting radionuclides, several alpha- and beta-particle emitters, and hypothetical emitters of monoenergetic electrons. The radionuclides of interest in this work are not included. The general conclusion regarding beta emitters is that, when all cells in a group are labeled, the internuclear component of the total dose is dominant irrespective of the number of cells in the group and increases as this number increases. It should be noted though that the authors examined energetic beta emitters used in radiotherapy of tumors such as ^{90}Y, ^{32}P, etc. Their statements might not be true for the radionuclides considered in this work, as one would expect internuclear dose to play less significant role for much less penetrating β particles of ^{3}H and ^{14}C. The problem of intranuclear dose versus internuclear dose therefore requires careful evaluation.

CHAPTER 3. METHODS

Model of a cell nucleus

The group working on the biological portion of this project has proposed to use low-passage human fibroblasts AG1521/1522 in the experiments. After these cells grow to confluence, they contact inhibit and enter a non-cycling G0 phase. In this monolayer state cells do not overlap to any extensive degree. This is an important condition for the experiments, because, if there were considerable overlapping, the internuclear dose component would be a confounding factor.

The results of measurements of nuclear sizes are reported in the literature for AG1522: the cross-sectional area of 144±45 μm^2 (*42*), the nuclear width of 9.4 μm (*13*), and the thickness of 1.1 μm (*13*). The biology group has undertaken measurements of nuclear dimensions for AG1521 cells. Fluorescence microscopy of plan images of cell nuclei yielded the following values: major axis of 23.1±2.7 μm and minor axis of 11.2±1.9 μm. Preliminary results of thickness measurements obtained by confocal microscopy indicated values of 2 – 2.5 μm. These results demonstrate that AG1521/1522 cells have very flat, "pancake-shaped" nuclei. It appears reasonable to consider a cell nucleus to be shaped as an ellipsoid, which is described by the following equation:

$$\frac{x^2}{a^2}+\frac{y^2}{b^2}+\frac{z^2}{c^2}=1\ , \tag{9}$$

where a, b and c are the ellipsoid semi-axes.

This model possesses a great flexibility as it can be easily modified to describe a wide variety of shapes including the special cases: 1) oblate spheroid, if $a = b > c$, or 2) sphere, when $a = b = c = R$. In the latter case,

$$x^2 + y^2 + z^2 = R^2 \ , \tag{10}$$

where R is the sphere radius.

As this project evolves, the above-mentioned morphometric results might need re-evaluation by the biology group to obtain the most realistic estimates for the values of a, b, and c for the finalized cell line and specific conditions in use.

β-particle spectrum

When one of the neutrons in the nucleus of an atom is transformed into a proton, beta particles (electrons, β^- or positrons, β^+) are emitted. Both radionuclides of interest in this work are pure electron emitters. β^- decay is accompanied by the emission of a neutrino:

$$n \rightarrow p + \beta^- + \nu \tag{11}$$

The total energy released in any decay is distributed between proton, electron and neutrino, which results in a distribution of electron energies characterized by the maximum energy, E_{max}, and the average energy, $\overline{E}$ (see Table 1 for the values of E_{max}

and $\overline{E}$ for ^{3}H and ^{14}C). The knowledge of beta spectra is important as an input to dosimetric calculations.

The allowed-shape spectra with Fermi correction were calculated for the two radionuclides with the following equations (*43*):

$$N(W) = p \cdot W \cdot (W_0 - W)^2 \cdot F(Z,W) \tag{12}$$

where $N(W)$ is the relative number of β particles per MeV,

W is the total energy of the electron (kinetic energy + $m_e c^2$) in units of $m_e c^2$,

W_0 is the corresponding value at the maximum electron energy,

$p = (W^2 - 1)^{1/2}$ is the electron momentum in units of $m_e c^2$,

m_e is the electron mass and c is the velocity of light,

Z is the atomic number of the daughter nucleus,

$F(Z,W)$ is the Fermi factor.

The Fermi factor accounts for the distortion of the spectrum by a Coulomb force between the nucleus and the emitted electron. For values of Z up to about 30, a good approximation for $F(Z,W)$ is

$$F(Z,W) = 2 \cdot (1+x) \cdot (2pR)^{2x-2} \cdot e^{\pi y} \cdot \frac{|\Gamma(x+iy)|^2}{(\Gamma(2x+1))^2} \tag{13}$$

where $x = [1 - (\alpha Z)^2]^{1/2}$,

$\alpha = 1/137.04$ is the fine structure constant,

$y = \alpha ZW/p$,

R is the nuclear radius in units of the Compton wave length of the electron (3.86×10^{-13} m),

$\Gamma(x+iy)$ is the complex gamma function.

An easily-calculated approximation for $|\Gamma(x+iy)|^2$ that has adequate accuracy for beta spectra calculations can be written as

$$|\Gamma(x+iy)|^2 = \frac{\pi y_1 (1+y_1^2)}{a^3 (x^2+y^2)\sinh \pi y_1} \cdot \exp\left[(1-x)\left[2 - \ln b + y_1 \tan^{-1}\left(\frac{y_1}{2}\right) + \frac{1}{6ab}\right]\right] \quad (14)$$

where $a = 2/(1+x)$, $y_1 = ay$ and $b = (1+x)^2 + y^2$.

The rejection method (*44*) was utilized to write a subroutine generating random energies from the spectra of ^{3}H and ^{14}C. Sample distributions obtained with the subroutine output are compared in Fig. 2 with theoretical curves calculated according to equations 12-14.

Monte Carlo simulation of electron track-structure

With the recent advent of powerful modern computers the use of Monte Carlo methods in various fields has increased dramatically. The term "Monte Carlo methods" refers to a mixture of techniques the common feature of whose is employing random numbers for modeling natural processes that are intrinsically stochastic. One of the first applications of Monte Carlo techniques was simulation of ionizing-particle transport through matter.

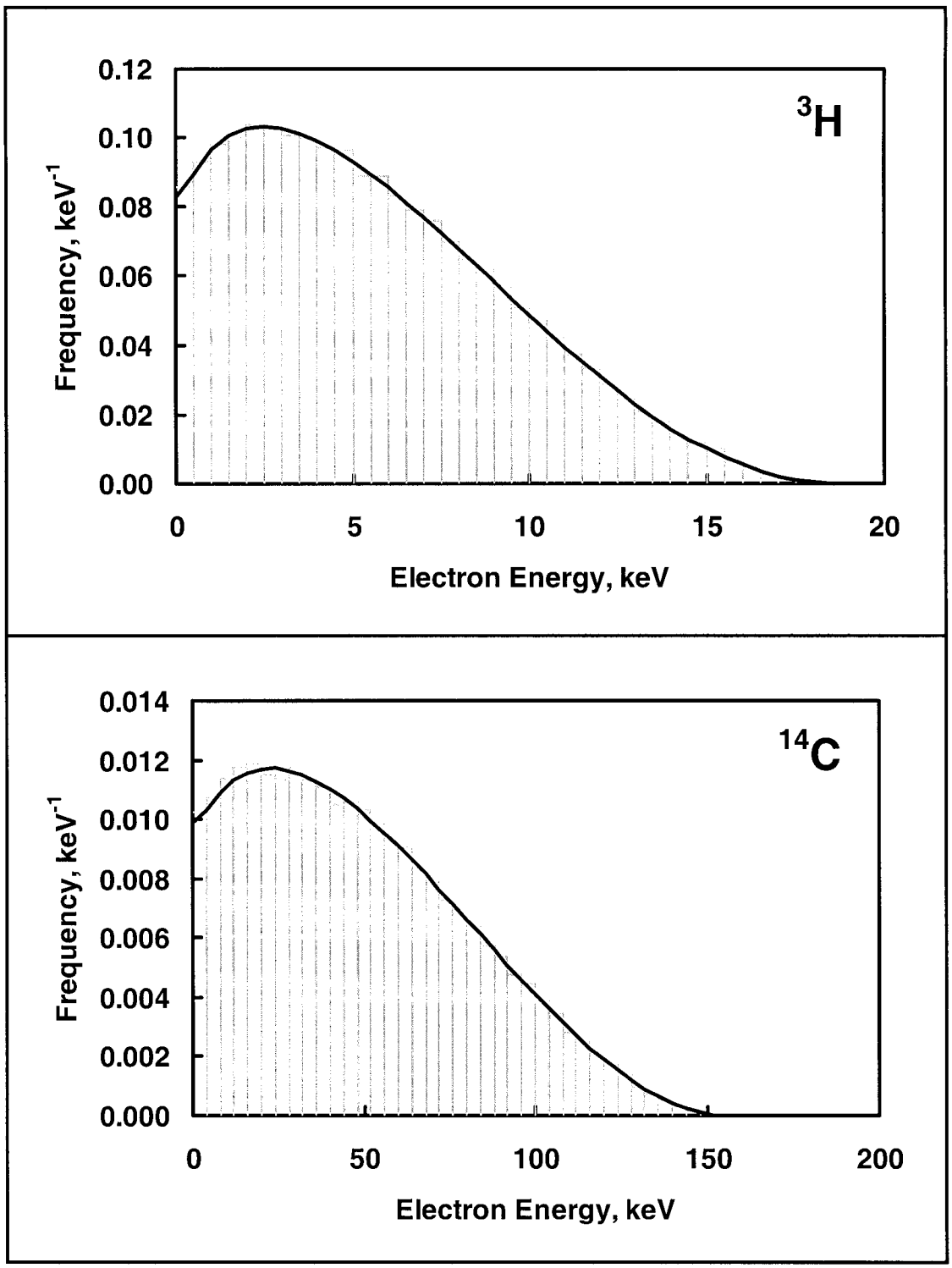

Figure 2. Spectra of ^{3}H and ^{14}C. The histograms are generated by the subroutine based on 100,000 β-particle energies each. The smooth lines are theoretical spectra. All curves and histograms are normalized to the area of unity.

Historically, first to appear were so called condensed-history (also referred to as multiple-scattering) Monte Carlo codes. These transport codes used theoretical distributions of energy loss and angular scattering in slabs of matter to determine the average energy deposited in relatively large volumes along the path of a particle and were particularly appropriate for transport of high-energy particles. The growing interest in understanding radiobiological damage on a DNA level required new models capable of simulating energy deposition processes on a micrometer, or even nanometer scale. That is why there is a shift towards developing and using detailed-history (single-scattering) Monte Carlo transport codes in the past three decades.

Such codes are based on cross-section data, which describe probabilities of different types of collisions of an ionizing particle with single atoms and molecules constituting the medium. In order to correctly describe naturally occurring processes, realistic cross sections have to be incorporated into a Monte Carlo code. These cross sections are either measured or derived from theoretical models. Currently, an abundance of information exists on cross sections for water vapor. However, in applications related to understanding biological effects of radiation, the processes of interest are those that occur in components of a biological cell (e.g., DNA). Unfortunately, a large portion of such data has never been measured or remains uncertain. The best approximation so far is simulations of particles' track structure in liquid water, despite that the knowledge of cross sections for the liquid phase is still scarcer than that for water vapor. As long as the most realistic input data are employed, single-scattering Monte Carlo codes are capable of simulating the finest details of track structure. They remain to be indispensable tools

for biophysical modeling at low energies down to eV region and on a small, nanometer scale, where direct measurements are impossible.

In this work, relating to beta dosimetry, the particular interest is in *electron* track-structure simulation. To date, a number of single-scattering Monte Carlo track-structure codes have been developed by a number of investigators to simulate physical and chemical processes created by electrons in both gaseous and liquid water (for the comprehensive overview see *35, 45*).

The Oak Ridge Electron Code (OREC) (*46-48*) was one of the first codes developed for liquid water. The code simulates the physical events that occur locally in a track segment within ~10^{-15} s after the passage of an electron. The products formed are excited and ionized water molecules and subexcitation electrons. Later the code RADLYS (*49, 50*) has been developed to simulate subsequent formation and spatial distribution of chemical species (OH, H_3O^+, H, H_2, O, and hydrated electrons) until ~10^{-6} s, when the chemical evolution of an electron track is essentially complete. OREC has been extensively used for solving problems in radiation chemistry (*51-56*), biophysical modeling (*57-62*) and health physics (*63, 64*). Recently, we (V. A. Semenenko, J. E. Turner and T. B. Borak) have undertaken efforts to revisit certain aspects of OREC. The revised code, called NOREC (see Appendix), is used in this work as the primary tool for investigating dosimetric problems of interest.

It was also possible to obtain samples of monoenergetic electron tracks with energies up to 150 keV generated by the liquid phase code PARTRAC (*65, 66*) and the water vapor code KURBUC (*67*). These data were used to determine whether different Monte Carlo codes would produce the same results.

In principle, track-structure codes transport a primary electron and all secondary electrons while recording the location, type of interaction, energy deposited, and other information for each event. For dosimetry problems, it is necessary to know the average energy absorbed within a volume of interest. If boundaries of the volume can be described mathematically, it becomes a trivial task with the use of Monte Carlo track-structure codes to follow every interaction of an electron and accumulate energy depositions associated with those interactions that occur within the volume. Repeating this procedure a large number of times and averaging the results gives a value for the average absorbed energy. The latter is then converted to dose by dividing by the mass of the volume. The diagram illustrating dose calculations is shown in Fig. 3, where several 10-keV electron tracks are superimposed on a 6-μm-diameter sphere. Assuming homogeneous labeling, all tracks originate uniformly and isotropically within the sphere.

Clustering analysis

When an electron loses its energy, the mean free path between interactions decreases and large angular deflections become more likely. These two phenomena are responsible for a higher density of interactions toward the end of an electron track. As opposed to higher-energy electrons that travel more or less along a straight path, low-energy electrons "wander around" thus forming *clusters* of energy depositions. Insofar as such clusters are the main focus of this research, we intend to undertake rigorous analyses to characterize them and to score frequencies of energy deposition by such events.

Clustering of data is a method by which a large set of data is organized into smaller groups whose members are similar in some way. Distance is really a measure of

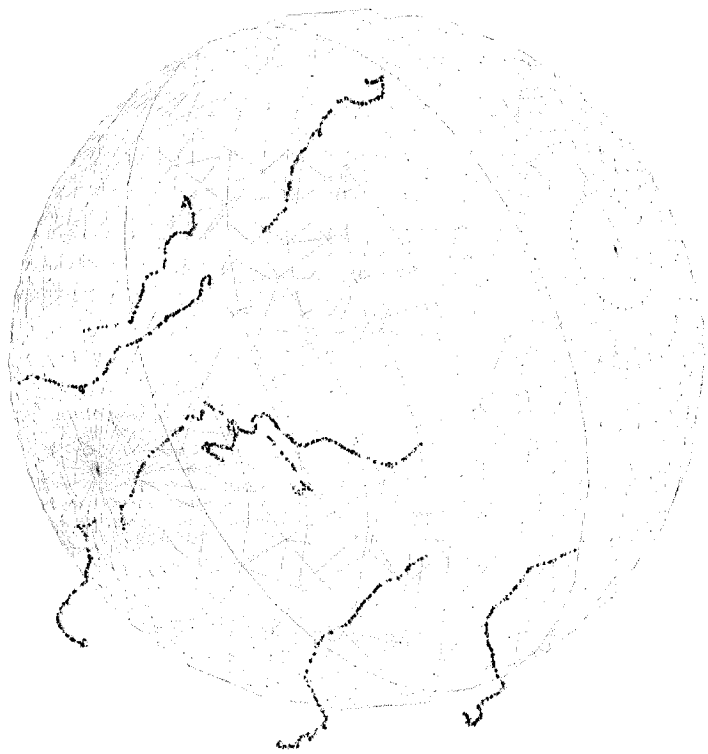

Figure 3. Calculations of energy deposited in a spherical cell nucleus with the use of a Monte Carlo track-structure code. Several 10-keV electrons originate uniformly and isotropically inside the 6-μm-diameter sphere.

similarity. Although alternative metrics are sometimes used in clustering analyses (Manhattan distance, maximum distance, etc.), Euclidean distance is the most typical. Since data to be analyzed in this work are spatial coordinates, it is natural to use Euclidean metric as a distance measure.

Perhaps the most widely used method here is the *K*-means clustering algorithm (*68-70*). This technique was used in several previous studies that employed track-structure calculations for modeling radiation damage processes (*35-37, 40*). The *K*-means method partitions N data points into K disjoint subsets, S_j, containing N_j data points. Let x_n be the vector of coordinates (dimension is not specified) representing nth data point. The algorithm proceeds as follows:

1. Choose K seeds ($K \leq N$) representative of initial cluster locations. There is no specific recipe for the initial partition; usually K points are picked at random.
2. Assign all the points in a data set to the nearest initial seed.
3. Calculate centroids. The centroid of a cluster S_j is a point whose coordinates are the mean of the coordinates of all the points in the cluster:

$$\mu_j = \frac{1}{N_j} \sum_{n \in S_j} x_n \tag{15}$$

4. Transfer data points between clusters so as to minimize the within-cluster sum of squares criterion:

$$J = \sum_{j=1}^{K} \sum_{n \in S_j} \left\| x_n - \mu_j \right\|^2 \tag{16}$$

When switching occurs, the centroids of both modified clusters are recalculated.

5. Repeat step 4 until no movement of a point from one cluster to another can reduce the within-cluster sum of squares.

In general, the *K*-means method does not achieve a global minimum for within-cluster sum of squares, but it is guaranteed to converge to a local optimum. The output from a clustering algorithm is basically a description of the cluster centroids with the number of components in each cluster.

The main drawback of the *K*-means clustering algorithm is that the number of clusters, *K*, has to be pre-assigned. Normally, one does not know *a priori* how many clusters there are in a data set. It is always desirable though to find compact and well separated clusters. The common approach to solving this problem is to repeat partition for different values of *K*. A criterion is then developed that reflects the "goodness" of clusters and behavior of this criterion as a function of *K* is investigated. Depending on the form of a criterion, the best *K* can be the value that either minimizes the function or maximizes it, or the value at which the function has a sharp knee. It should be noted that there is still a great amount of subjectivity in choosing both appropriate criterion and optimal number of clusters. There is one study (*71*) that compares 30 cluster validation criteria described by different authors. One of the basic conclusions is that the performance of such criteria may be data dependent.

In this research, a modified version of the *K*-means clustering algorithm is used. The suggestion of Michalik (*36, 37*) is adopted to require that every member of a cluster be not farther away from all other members than some distance *p*, which will be referred to as cluster parameter:

$$\|x_k - x_l\| \leq p \quad \forall k,l \in S_j \tag{17}$$

This approach has the following advantages: 1) the approximate spatial characteristics of clusters are known by default; 2) the choice of p automatically defines the number of clusters K for any particular electron track. Thus, the problem of obtaining "good" clusters converts from having to find the valid value of K to searching for optimal p. To obtain the initial partition, data set is scanned in order and first N_1 points satisfying the condition in equation 17 are recorded as belonging to cluster S_1 and so on until all data points are partitioned. Then cluster members are relocated according to the step 4 in the original algorithm. Clusters are allowed to collapse, which happens when all the data points in one cluster can be moved to other clusters.

A computer program implementing the described algorithm was written. The program takes cluster parameter p and a table of spatial coordinates of electron interactions along with corresponding energy depositions as input parameters and returns a table of coordinates of cluster centroids, energy deposited by each cluster, and the number of interactions in each cluster.

CHAPTER 4. RESULTS AND DISCUSSION

Comparison of results for spherical nuclei

Many studies involving incorporated radionuclides were performed in 1960s and early 1970s. Most of work on dosimetry of such radionuclides also dates back to this period. Since then, new means for solving dosimetric problems have appeared, namely Monte Carlo particle-transport codes. These have proven to be powerful tools capable of not only calculating energy deposited in a target per se, but also determining patterns of energy deposition within volumes of interest, estimating their microdosimetric characteristics. In this section, results produced by previously used methods for dose calculation from ^{3}H and ^{14}C incorporated into a cell nucleus are compared with results obtained with Monte Carlo track-structure codes.

As described above, an overwhelming majority of early studies on evaluation of doses from incorporated radionuclides were accomplished under the assumption of spherical geometry. Therefore comparisons are made for spherical nuclei and results are expressed as functions of sphere radius. Spheres with radii up to 20 μm are considered.

It is convenient to compare results in terms of absorbed fractions. The absorbed fraction is a portion of the average energy of β particles, $\overline{E}_{\beta}$, that is absorbed inside a nucleus:

$$F = \frac{\overline{E}_{abs}}{\overline{E}_{\beta}} \tag{18}$$

As $\overline{E}_{abs}$, the absorbed fraction depends on emission spectrum of a radionuclide and the dimensions of a volume, for which it is defined. It is obvious that F is an increasing function of those dimensions. With the use of the absorbed fraction concept, the absorbed dose to a spherical volume of radius R can be written as

$$D = \frac{\overline{E}_{abs}}{m} = \frac{F(R) \cdot \overline{E}_{\beta}}{\rho(4/3\pi R^3)} \tag{19}$$

Supplying numerical values for equation 19 (assuming $\rho = 1$ g/cm^3) gives:

$$D[Gy/dis] = 3.82 \cdot 10^{-2} \frac{F(R)}{R^3} \overline{E}_{\beta} \ , \tag{20}$$

where R is in microns and $\overline{E}_{\beta}$ is in keV. The absorbed fraction, F, is the only unknown in equation 20. The problem of beta dosimetry in a cell nucleus is thus reduced to finding the function $F(R)$.

A description of methods used in comparisons for both radionuclides is as follows.

Tritium

Method 1. Point kernel of Robertson *et al.* (*23*) (eq. 1). If a point kernel for a beta emitter is known, the absorbed fraction can be found as a ratio of two integrals: the integral of the point kernel over the volume of a sphere, I_1, representing the average energy absorbed in the sphere per disintegration, and the integral over entire space, I_2,

giving the average energy emitted by the radionuclide per disintegration. The result of the integration of Robertson's point kernel is known from the literature (*15*):

$$I_1 = \frac{8\pi}{16.02}\sum_{i=1}^{2}\frac{c_i}{k_i^3}\left\{1-\frac{3}{4k_i^3R^3}\left[e^{-2k_iR}\left(2k_i^3R^3+7k_i^2R^2+10k_iR+5\right)+3k_i^2R^2-5\right]\right\}, \quad (21)$$

where 16.02 is the conversion factor from keV/μm^3 to rad (assuming density of 1 g/cm^3);

c_1 = 185 rad/dis, c_2 = 15 rad/dis, k_1 = 5.55 μm^{-1}, and k_2 = 1.92 μm^{-1}.

The integral over entire space

$$I_2 = \frac{4\pi}{16.02}\int_0^{\infty} r^2 D(r)dr = \frac{8\pi}{16.02}\left(\frac{c_1}{k_1^2}+\frac{c_2}{k_2^2}\right) \quad (22)$$

yields 5.02 keV for the average energy emitted by ^{3}H, which underestimates the conventional value of 5.7 keV. The ratio I_1 / I_2 then gives the absorbed fraction.

Method 2. Point kernel given by Goodheart (*24*). Equation 6 was integrated over the geometrical reduction factor for a sphere of radius R (*27*)

$$\Psi(x) = \begin{cases} 1-\frac{3}{4}\left(\frac{x}{R}\right)+\frac{1}{16}\left(\frac{x}{R}\right)^3 & 0 \le x \le 2R \\ 0 & x > 2R \end{cases} \quad (23)$$

to obtain the energy absorbed inside the sphere:

$$I_1 = \frac{4\pi}{16.02}\int_0^{\infty} r^2 \Psi(r) D(r) dr$$

$$= \frac{4\pi}{16.02}\cdot\frac{3}{\gamma}\left\{10\alpha\tan^{-1}(20R) + \sqrt{10}\beta\tan^{-1}(\sqrt{0.4}R) + \sqrt{5}\chi\tan^{-1}(\sqrt{0.8}R) - \right.$$

$$-\frac{3}{8R}\left[\alpha\ln(400R^2+1) + 10\beta\ln(0.4R^2+1) + 5\chi\ln(0.8R^2+1)\right] +$$

$$\left. +\frac{1}{32R^3}\left[\delta\ln(400R^2+1) + 10\varepsilon\ln(0.4R^2+1) + 5\phi\ln(0.8R^2+1)\right]\right\} \qquad (24)$$

where $\alpha = -0.001$; $\beta = -0.0998$; $\chi = 0.1998$; $\delta = 0.00001$; $\varepsilon = 0.998$; $\phi = -0.999$, and $\gamma = 0.0997002$.

The integral of equation 6 over entire space

$$I_2 = \frac{4\pi}{16.02}\cdot\frac{3}{\gamma}\cdot\frac{\pi}{2}\left(10\alpha + \sqrt{10}\beta + \sqrt{5}\chi\right) \approx 4.49\,keV \qquad (25)$$

considerably underestimates the average energy of β particles emitted by ^{3}H, 5.7 keV. The absorbed fraction, F, was then obtained as a ratio of I_1 and I_2.

Method 3. Point kernel of Stewart (*25*). This is a classic exponential point kernel (eq. 2) with $1/\mu = 1.5$ μm. The integral over a sphere is also reported in (*15*):

$$I_1 = \overline{E}_\beta\left[1 - \frac{3}{4\mu^3R^3}\left\{e^{-2\mu R}\left(\mu R + \frac{1}{2}\right) + \mu^2R^2 - \frac{1}{2}\right\}\right] \qquad (26)$$

The integration over all space gives $I_2 = \overline{E}_\beta$. Thus, the absorbed fraction for a sphere can be written as

$$F(R) = 1 - \frac{3}{4\mu^3 R^3}\left\{e^{-2\mu R}\left(\mu R + \frac{1}{2}\right) + \mu^2 R^2 - \frac{1}{2}\right\} \tag{27}$$

Method 4. The expression for the average dose absorbed in a spherical cell nucleus obtained by Apelgot and Duquesne (*32*) (eq. 7) can be easily converted into the absorbed fraction for the sake of comparison:

$$F(R) = 0.876 + 0.124\left(\frac{R-1}{R}\right)^3 \quad \text{for } R \geq 2\ \mu\text{m} \tag{28}$$

Method 5. Monte Carlo electron track-structure code NOREC (Appendix). 100,000 electron tracks with initial energies from tritium β spectrum were generated and placed uniformly and isotropically inside a sphere. Each electron history was followed to the end in order to score the amount of energy deposited by an electron inside the sphere (eq. 10). For each electron, the initial electron energy and the energy deposited in the sphere were recorded and then averaged over 100,000 electrons. The ratio of the average deposited energy to the average emitted energy gives the fraction of energy absorbed in the sphere. The calculation was repeated for spheres of different size.

Method 6. Monte Carlo electron track-structure code PARTRAC (*65, 66*). The direct calculation of the average energy deposited by ^{3}H described above was not possible in

this case, because electron tracks with continuous beta energies were not readily available. Instead, samples of 200 electron histories with the following energies: 1, 3, 5, 6, 7, 8, 9, 10, 12, 15, 20, 30, 50, 80, 100, 120, and 150 keV were utilized in the calculation. For each initial energy, the average energy deposited by electrons in spheres of different radius was calculated and the data were fitted with smooth curves. The calculated data for initial electron energies up to 150 keV along with the fits are shown in Fig. 4. The fitted curves were then numerically integrated over the normalized spectrum of ^{3}H (Fig. 2) to find the average energy deposited by tritium for each sphere size. Dividing these values by the average beta energy gives absorbed fractions.

Method 7. Monte Carlo electron track-structure code KURBUC (*67*). Electron tracks with energies 1, 3, 5, 6, 7, 8, 9, 10, 15, 20, 30, 50, 80, and 100 keV (200 histories each) generated by the code KURBUC were available for calculation. The method of computation of absorbed fractions is the same as above. The average energy deposited in spheres of different radius as a function of electron energy and the fitted curves are shown in Fig. 5.

Absorbed fractions for ^{3}H obtained by described methods are presented in Fig. 6. It was pointed out by Shiragai (*16*) that doses calculated by Apelgot and Duquesne (method 4) are expected to be overestimated. The results obtained by method 2 also have little credibility. These are from the fit provided by Goodheart (*24*) to the earlier data of Robertson and Hughes (*22*). As it was demonstrated above, Goodheart's equation significantly underestimates the average β-particle energy of tritium and therefore it should be rejected in favor of other fits to the same data (methods 1 and 3) that provide better agreement.

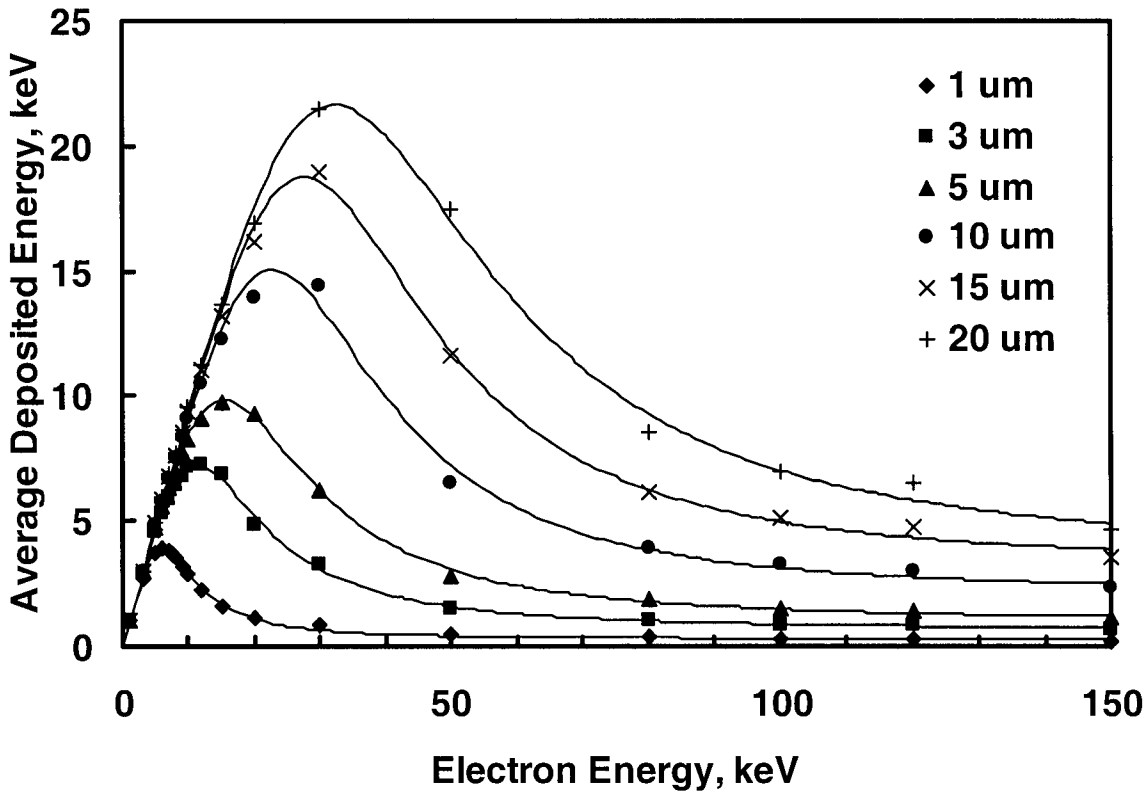

Figure 4. Average energy deposited in spheres of different size calculated with the Monte Carlo code PARTRAC (*65, 66*) as a function of electron energy. Sphere radii are given in the legend. The lines are least-squares fits to the calculations.

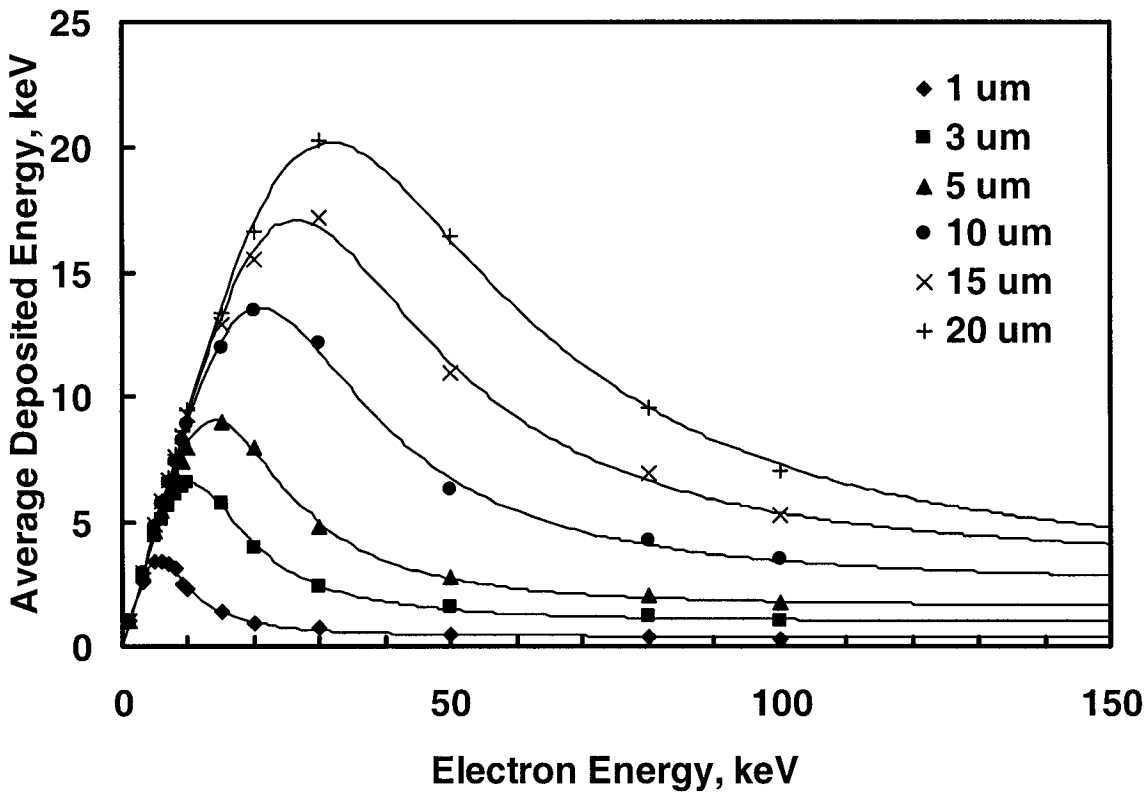

Figure 5. Average energy deposited in spheres of different size calculated with the Monte Carlo code KURBUC (*67*) as a function of electron energy. Sphere radii are given in the legend. The lines are least-squares fits to the calculations.

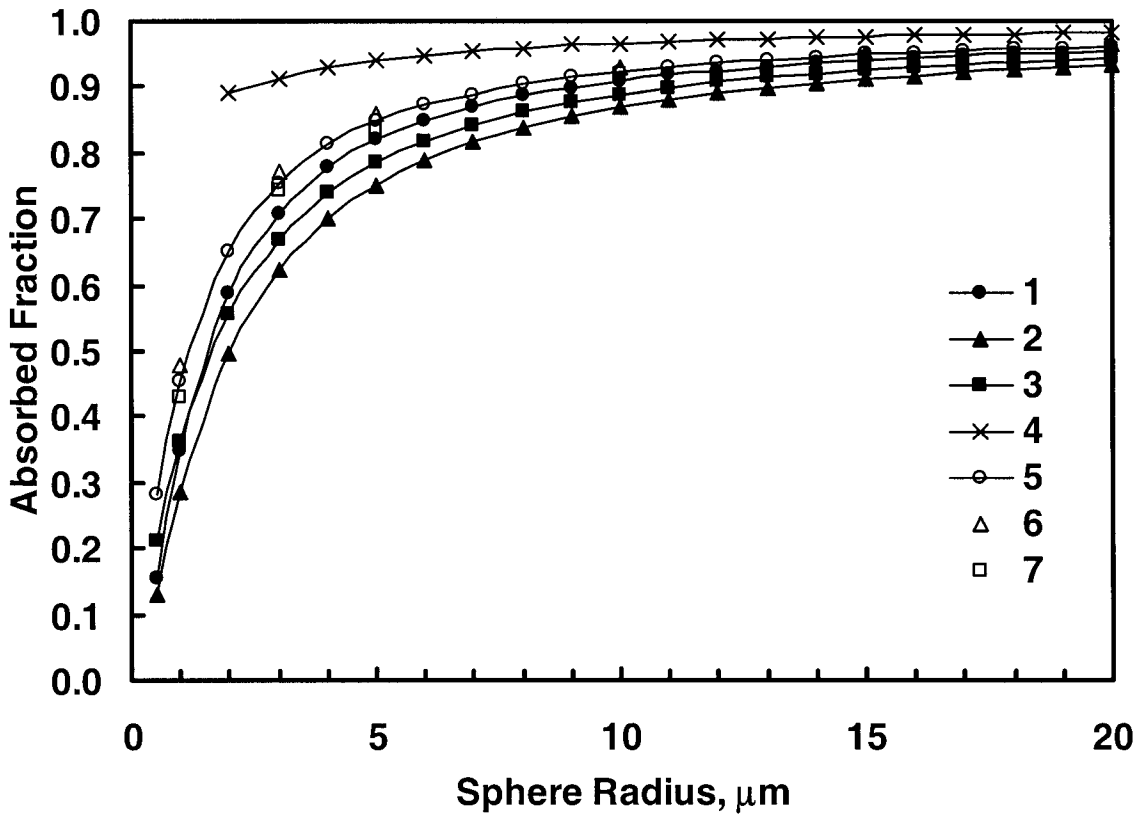

Figure 6. Absorbed fraction for ^{3}H uniformly distributed in spherical volumes. 1 – point kernel of Robertson *et al.* (*23*), 2 – point kernel of Goodheart (*24*), 3 – point kernel of Stewart (*25*), 4 – method of Apelgot and Duquesne (*32*), 5 – Monte Carlo code NOREC (Appendix), 6 – Monte Carlo code PARTRAC (*65, 66*), 7 – Monte Carlo code KURBUC (*67*).

Carbon-14

Method 1. This and next methods are based on the point kernel described by equation 2 with the minimal and maximal values of the absorption coefficient for ^{14}C reported in Table I of (*15*). The absorbed fraction in this case is given by equation 27 with $\mu = 0.0213\ \mu m^{-1}$.

Method 2. The same as above, but using $\mu = 0.0295\ \mu m^{-1}$.

Method 3. The smallest energy, E_{max}, based on which Loevinger's model (*20*) was derived is 0.17 MeV (eq. 4). With a little extrapolation, the Loevinger's point kernel (eq. 3) can be applied to ^{14}C (E_{max} = 0.156 MeV). Integrating equation 3 over the geometrical reduction factor (eq. 23) and dividing by the integral over entire space, $I_2 = \overline{E}_\beta$, one obtains for the absorbed fraction:

$$F(R) = \frac{1}{c^2(3-e)+e}\left\{\frac{3}{4}cv + e\left[1 - \frac{3}{2v^3}\left(v^2 - 1 + e^{-2v}(v+1)^2\right)\right] - \right.$$

$$\left. - ec^2\left[1 - \frac{3}{2u^3}\left(u^2 - 1 + e^{-2u}(u+1)^2\right)\right]\right\}, \qquad (29)$$

where $c = 2$, $\mu = 0.034\ \mu m^{-1}$, $v = \mu R$, and $u = v/c$.

Method 4. Kühn (*33*) gives an example of the absorbed energy calculation by his method for ^{14}C incorporated into a sphere. He has found the average energy absorbed inside the 10-μm-radius sphere to be 8.28 keV. Then the absorbed fraction is $F(10\ \mu m)$ = 8.28 keV / 49 keV = 0.17.

Method 5. Monte Carlo code NOREC (Appendix). Energetic β particles produced by ^{14}C can travel as far as 300 μm (Table 1). This is several times more than the longest chord through the set of considered spheres, 40 μm (for the 20-μm-radius sphere). Such high-energy electrons deposit a relatively small amount of their energy inside a nucleus and, once they escape, they have a little chance of crossing the nucleus again and depositing additional energy. Providing that the time necessary to generate and follow an electron track increases nearly linearly with the electron energy, it becomes highly inefficient to follow entire electron histories in case of ^{14}C.

A following test was conducted. Electron tracks with a number of energies up to 160 keV (5,000 electrons of each energy) were generated originating uniformly and isotropically inside a 20-μm-radius sphere. A spherical shell surrounding the sphere was included in the computation. For each electron, the energy deposited inside the sphere was counted. Once an electron had exited the specified spherical shell surrounding the sphere, the value of energy deposited in the sphere was stored. The energies deposited in the sphere for 1-, 3-, 5-, and 10-μm-thick shells as well as "unrestricted" value (when entire electron histories are followed) were recorded. These values were averaged over 5,000 electrons and the percent of deposited energy that remains unaccounted was determined for every shell. The results are presented in Fig. 7. One can see that for a 10-μm-thick shell surrounding a 20-μm-radius sphere no more than 3% of energy deposition is lost when the track is terminated after exiting the shell. A 20-μm-radius sphere was used in this exercise since for realistic cell nuclei, there is even less chance that escaped electrons reenter a nucleus.

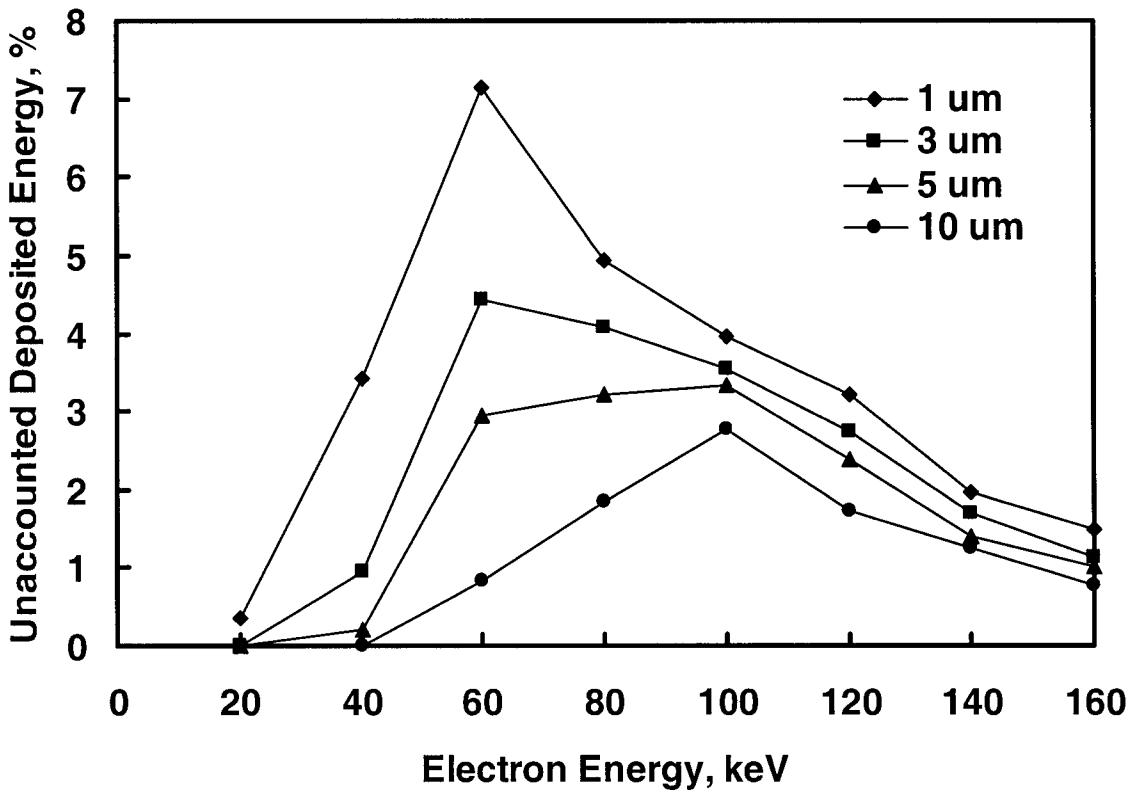

Figure 7. Percent of the average energy deposited in a 20-μm-radius sphere that remains unaccounted if following electron tracks is discontinued when they escape 1-, 3-, 5-, and 10-μm-thick shells surrounding the sphere.

Thus in NOREC calculations for ^{14}C, generation of electron tracks was discontinued upon their escaping 10-μm spherical shell around nuclei and 3% is believed to be the upper limit for the error introduced by employing such technique.

Method 6. Monte Carlo code PARTRAC (*65, 66*). The calculation procedure for this and the next method is the same as for ^{3}H, except that the fitted curves in Figs. 4 and 5 were integrated over the ^{14}C spectrum.

Method 7. Monte Carlo code KURBUC (*67*).

As a test of validity of the technique for computation of average deposited energy used with PARTRAC and KURBUC data, an additional calculation with NOREC by such indirect method was undertaken. Table 2 demonstrates that the resulting average energies agree very well for the direct and indirect methods.

Table 2. Comparison of the average energy deposited by ^{3}H and ^{14}C in spheres of different size calculated with the Monte Carlo code NOREC using direct and indirect methods.

Sphere radius, μm	^{3}H		^{14}C	
	direct	indirect	direct	indirect
1	2.58	2.60	0.85	0.83
3	4.30	4.31	2.40	2.39
5	4.83	4.84	3.87	3.85
10	5.26	5.26	7.23	7.18
15	5.39	5.40	10.13	10.12
20	5.48	5.46	12.70	12.74

The advantage of the direct method is that it takes only one programming step to obtain final results, whereas the indirect method that requires tedious intermediate steps is suitable if there are gaps in data.

Fig. 8 shows absorbed fractions for ^{14}C calculated by the above-described methods. The data point obtained by method 4 is likely to be an overestimate. In this method, proposed by Kühn (*33*) and briefly described in the Literature Review, the mean distance up to which energy of β particles is fully absorbed is identified as $\overline{L} = 1.2R$. This is the mean of distribution of distances between uniformly distributed points inside the sphere and uniformly distributed points on the surface on the sphere. It is more reasonable though to use the distribution of the length of rays defined by isotropic directions from points uniformly distributed inside the sphere. The latter distribution is known as *i*-randomness (*72*). Its mean for a sphere of radius *R*, $\overline{L} = 0.75R$, is smaller than the distance used by Kühn, which would result in smaller values of the average deposited energy.

Unfortunately, there are no experimental data available to which results in this section could be compared. It is believed that Monte Carlo simulation of electron track structure provides the most credible information to date about energy deposition by low-energy radiations, such as ^{3}H and ^{14}C, in micrometer-sized targets. It is encouraging that results produced by three different Monte Carlo codes for both ^{3}H and ^{14}C agree within a few percent.

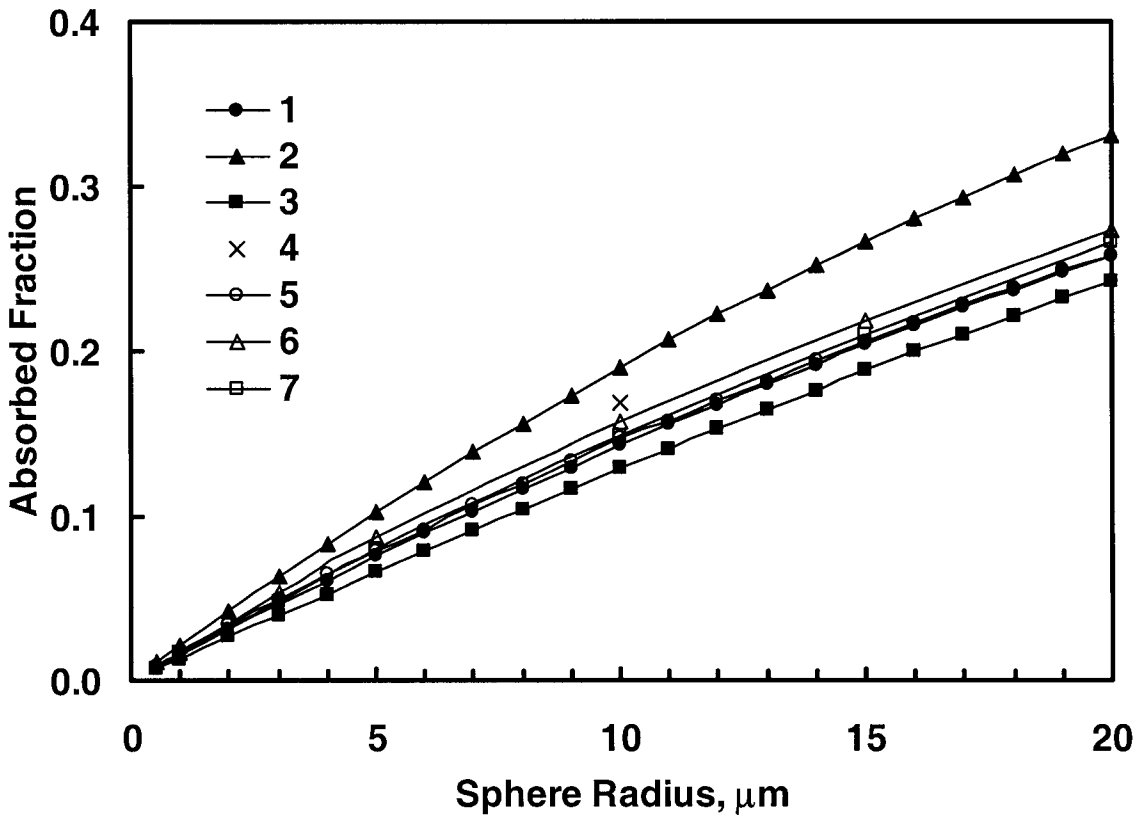

Figure 8. Absorbed fraction for ^{14}C uniformly distributed in spherical volumes. 1 – point kernel proportional to $e^{-\mu r}/r^2$ with $\mu = 0.0213$ μm^{-1}, 2 – point kernel proportional to $e^{-\mu r}/r^2$ with $\mu = 0.0295$ μm^{-1}, 3 – point kernel of Loevinger (*20*), 4 – method of Kühn (*33*), 5 – Monte Carlo code NOREC (Appendix), 6 – Monte Carlo code PARTRAC (*65, 66*), 7 – Monte Carlo code KURBUC (*67*).

Intranuclear dose

It was demonstrated in the previous section that different Monte Carlo track-structure codes yield consistent results for absorbed fractions and hence absorbed doses in a cell nucleus. Since we have unlimited access to the Monte Carlo code NOREC, which allows us to generate large sets of electron histories with a continuous spectrum of initial energies corresponding to ^{3}H and ^{14}C, this code will be used in the rest of the work. Fig. 9 shows absorbed dose to a spherical cell nucleus uniformly labeled with ^{3}H or ^{14}C. These results are based on the absorbed fraction calculated with NOREC for ^{3}H (Fig. 6) and ^{14}C (Fig. 8) and equation 20 to convert absorbed fraction to absorbed dose. The absorbed dose decreases for large nuclei because the volume (or the mass) of a nucleus increases faster than the average deposited energy.

While the interest of this research are estimates of absorbed dose for specific cells with ellipsoidal nuclei, it is more helpful to observe general behavior of dose as a function of some parameter, like that in Fig. 9. In biological experiments with cell cultures, the same type of cells can sometimes have different conformations. For example, cells in suspension tend to have a spherical shape and so do their nuclei, whereas plated cells and nuclei have more of an ellipsoidal shape. A model of a cell nucleus with such geometry is described as follows.

The starting point is a 6-μm-diameter sphere. This is often used as a model of an average mammalian cell nucleus. Imagine that this sphere is transformed into an oblate spheroid, without changing its volume (Fig. 10). If the short axis of the spheroid is t, which will be referred to as thickness, then the other two axes can be determined as

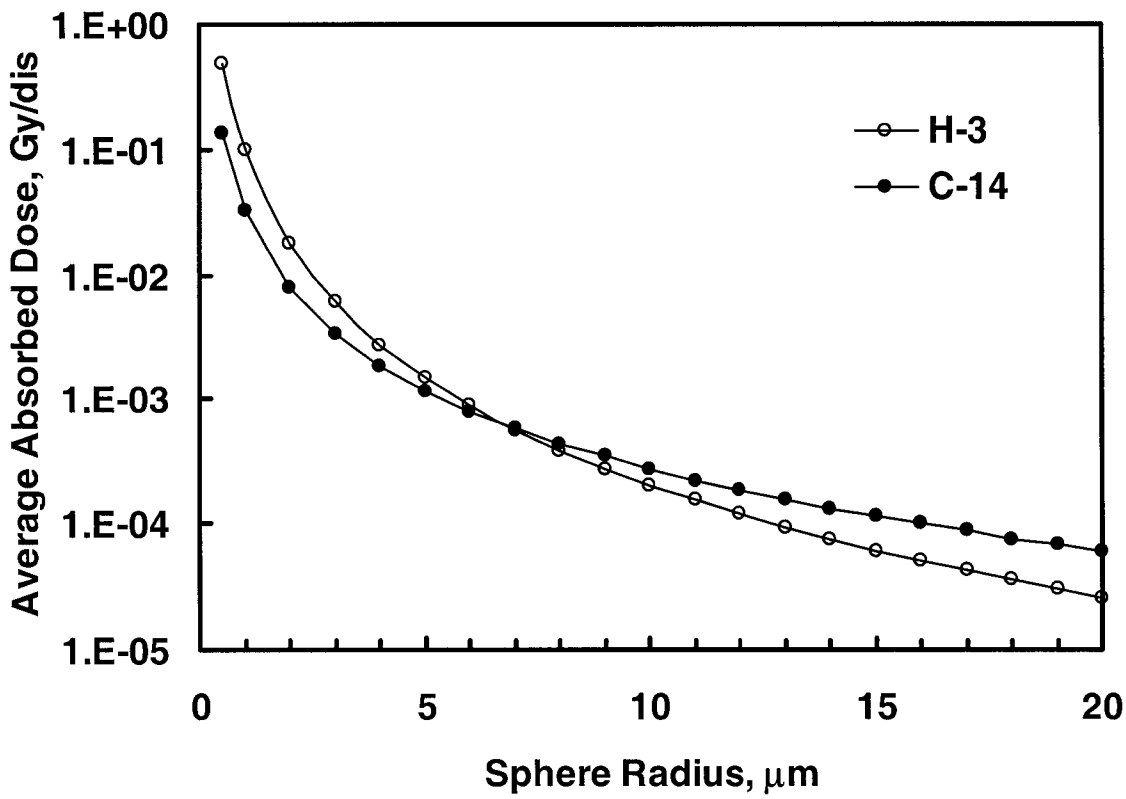

Figure 9. Average absorbed dose per disintegration due to ^{3}H and ^{14}C uniformly distributed in spherical cell nuclei.

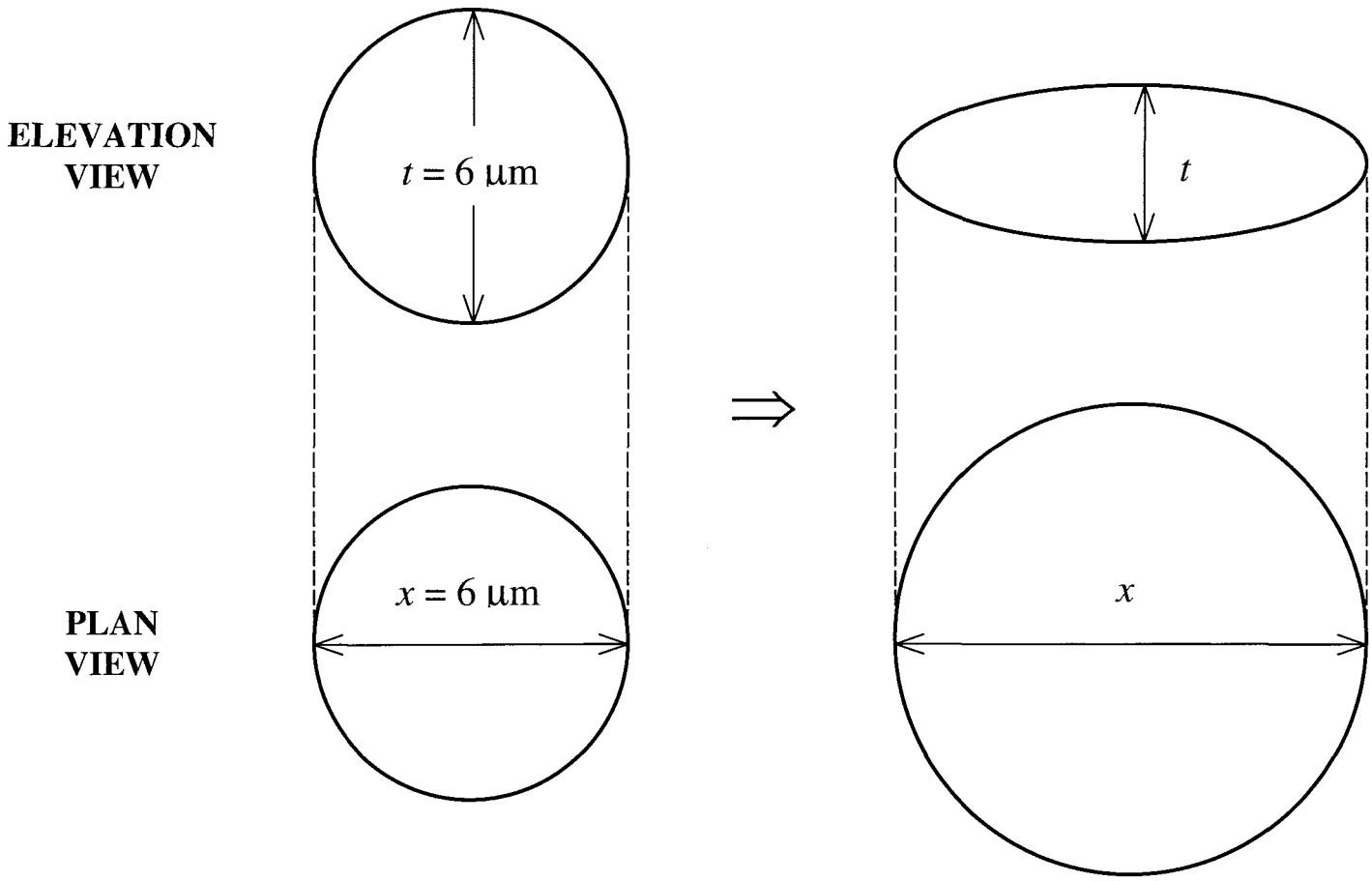

Figure 10. Flat nucleus model. From the 6-µm-diameter sphere on the left the nucleus is transformed to an oblate spheroid on the right. Specifying nuclear thickness, t, uniquely defines the other two dimensions, x.

$$\frac{4}{3}\pi\cdot(6/2)^3=\frac{4}{3}\pi\cdot\frac{t}{2}\cdot\frac{x}{2}\cdot\frac{x}{2}\Rightarrow x=\sqrt{\frac{3^3\cdot 8}{t}}\,, \tag{30}$$

where t and x are in microns and $0 < t \leq 6\,\mu m$. In this model, which will be referred to as "flat nucleus model", small values of t define a pancake-shaped nucleus, and the thickness of 6 μm corresponds to a spherical nucleus.

The average energy deposited by ^{3}H and ^{14}C in ellipsoids of different size described by equation 9 with $a = t/2$, $b = c = x/2$ and t varying between 0.5 and 6 μm was scored using the Monte Carlo code NOREC. The calculation procedure is the same as described in the previous section for spherical nuclei. In case of ^{14}C, electron histories were discontinued upon escaping a 10-μm-thick shell surrounding a nucleus. The results are shown in Fig. 11 as functions of nucleus thickness.

With little modifications, formula 20 can be used to calculate absorbed dose to an elliptical nucleus:

$$D[Gy/dis]=3.82\cdot 10^{-2}\frac{\overline{E}_{abs}}{abc} \tag{31}$$

where $\overline{E}_{abs}$ is in keV/dis and a, b, c are in μm. For the flat nucleus model, the product abc is constant and equals 27 μm^3. The absorbed doses due to ^{3}H and ^{14}C resulting from equation 31 are shown in Fig. 12. Because the nuclear volume remains the same, the absorbed dose increases as the average deposited energy.

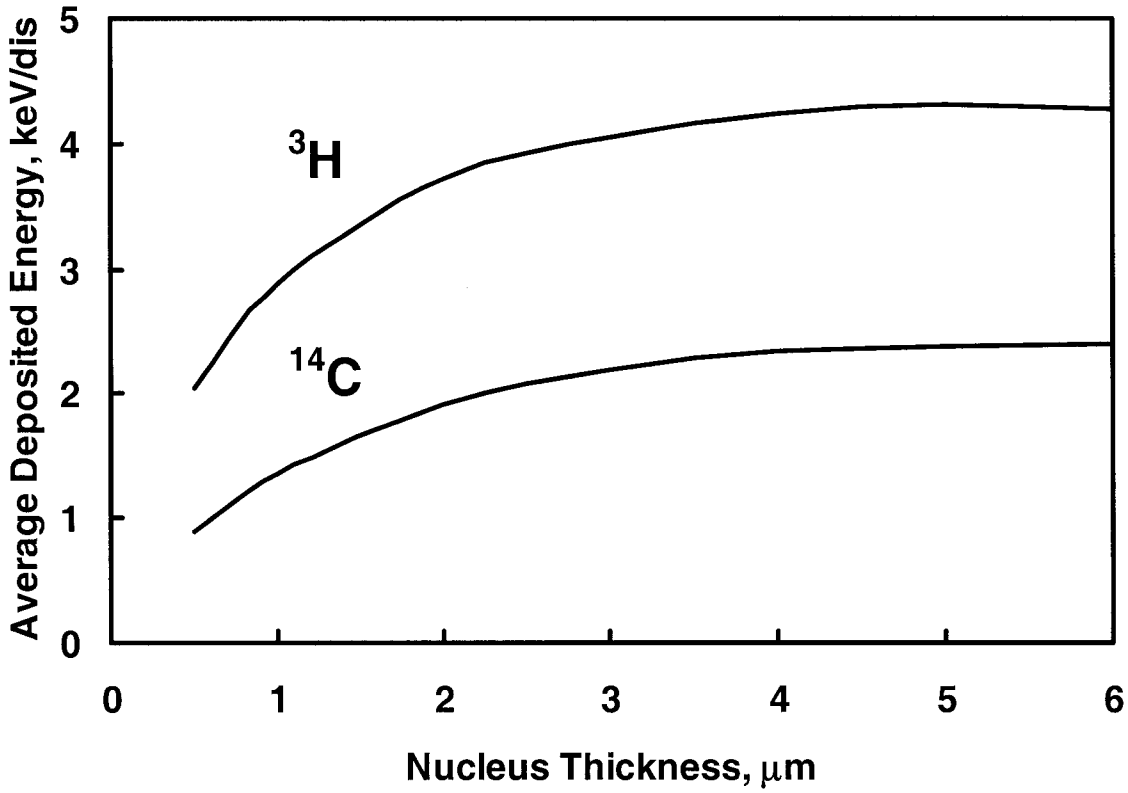

Figure 11. Average energy deposited in cell nuclei described by the flat nucleus model.

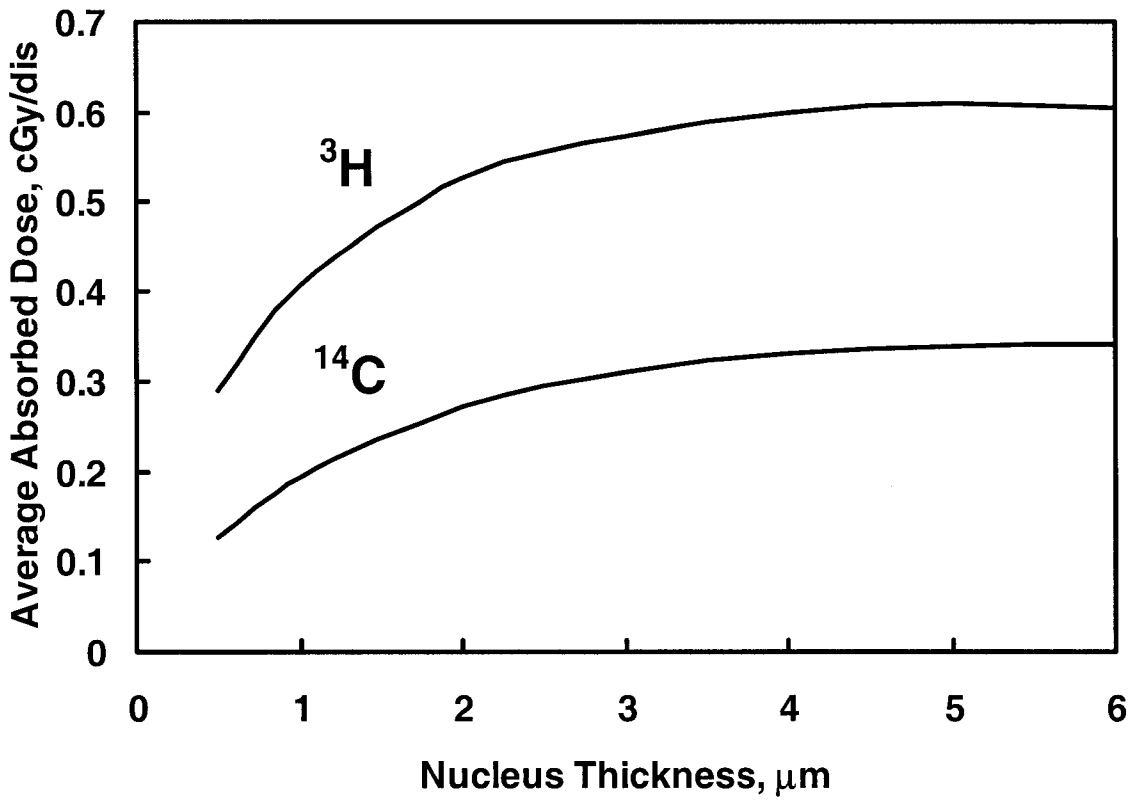

Figure 12. Average absorbed dose to cell nuclei described by the flat nucleus model.

Fraction of dose due to track-end clusters

In the previous section, the average dose to a cell nucleus per disintegration of ^{3}H or ^{14}C was computed for nuclei of different size and form. It is a critical goal of this research to estimate the fraction of this dose that is delivered by electron track ends in case of ^{3}H and ^{14}C. The end of an electron track is a rather vague notion indicating that there is something qualitatively different about the terminal part of an electron track compared with the rest of the track. Therefore the first step in this portion of the work is to develop a quantitative definition of track ends, which then can be used in scoring procedures in order to subdivide deposited energy into "low-LET" and "high-LET" parts.

The term "high-LET part of an electron track" is considered preferable to "electron track end", because the latter fails to take into account energetic secondary electrons that can occur far away from the actual track end. Such electrons are not in any way different from the slowing-down primary electron in terms of forming clusters of energy depositions and therefore would have the same relevance, if any, to biological damage. It should be realized that there is no clear border between "low-LET" and "high-LET" portions of electron tracks as well as any specific LET associated with these two concepts. Bearing in mind these limitations, the terms "low- / high-LET portion of electron tracks", "low- / high-LET energy deposition events", and "low- / high-LET clusters" will be used henceforth without quotation marks.

Since increased clustering of energy depositions is a characteristic feature of a high-LET portion of electron tracks, clustering techniques are considered appropriate tools for such investigation. The algorithm employed in this work is outlined in the Methods. A table of spatial coordinates corresponding to inelastic electron interactions

and energy deposited is generated with the Monte Carlo track-structure code. This table is entered into a *K*-means clustering algorithm along with a cluster parameter p. The output is a reduced table that contains the following information about each detected cluster: coordinates of cluster centroids, total energy deposited by the cluster (obtained by summing energy depositions in individual interactions), and the number of energy depositions in the cluster. The latter will be referred to as cluster order.

Cluster order and energy deposited by the cluster are highly correlated. One example is shown in Fig. 13 for one hundred 5-keV electrons partitioned using $p = 0.05$ μm. Dependences obtained for other electron energies and other values of p are similar. Consequent analyses will be conducted in terms of cluster order.

Due to applying the condition in equation 17, the algorithm yields clusters that can be described as spherically shaped convex polyhedra of characteristic "diameter" p. The parameter p has to be specified as an input for the clustering algorithm. The question arises as to what values are suitable for analysis. Consider the following argument. Fig. 14 shows the terminal part of a 5-keV electron track generated with NOREC. Each small circle represents the location of the energy deposition. There is a prominent high-LET track-end cluster. If p is too small (panel A), the actual high-LET cluster will be divided into smaller clusters like, for example, the cluster labeled 1. Such small clusters will be practically undistinguishable from clusters pertaining to low-LET portion of a track, such as the cluster labeled 2. If, on the contrary, p is too large, the resulting structure will erroneously contain some low-LET events along with the actual high-LET cluster (panel B). Therefore an optimal value of p exists for every particular high-LET

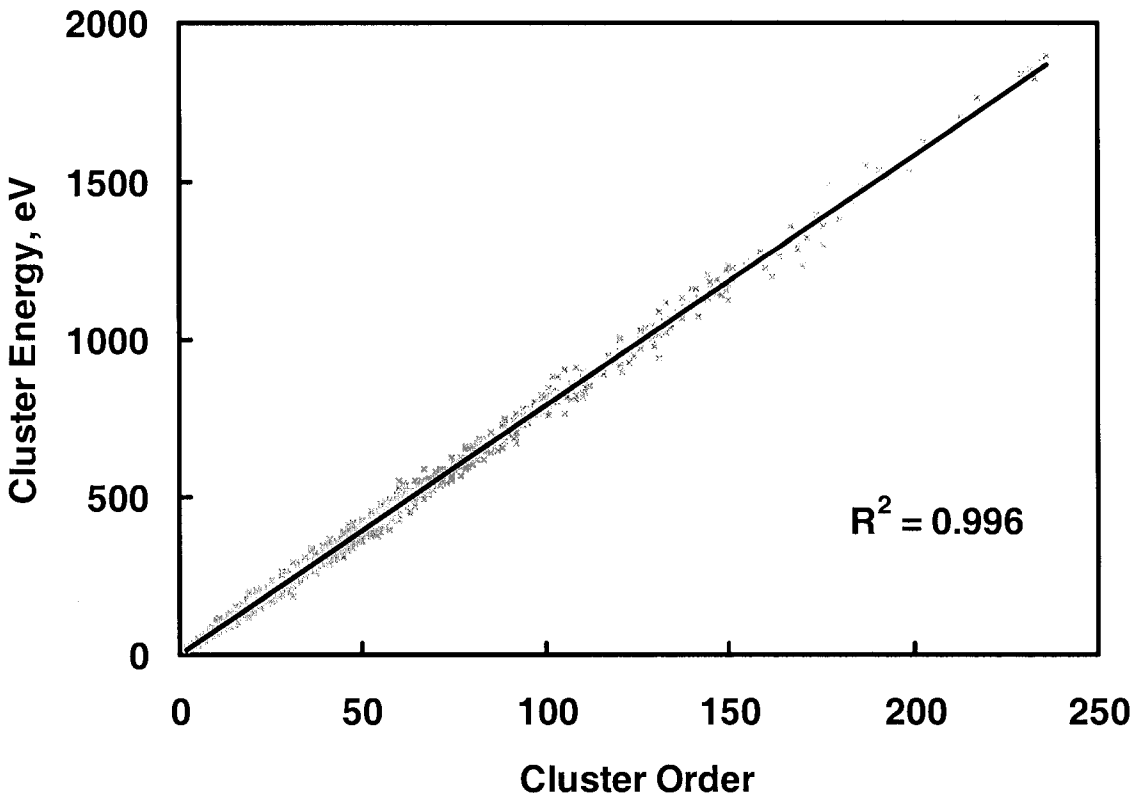

Figure 13. Correlation between cluster order and energy deposited by the cluster. The data are for one hundred 5-keV electron tracks partitioned using $p = 0.05$ μm. The linear trendline and the r-square value are shown.

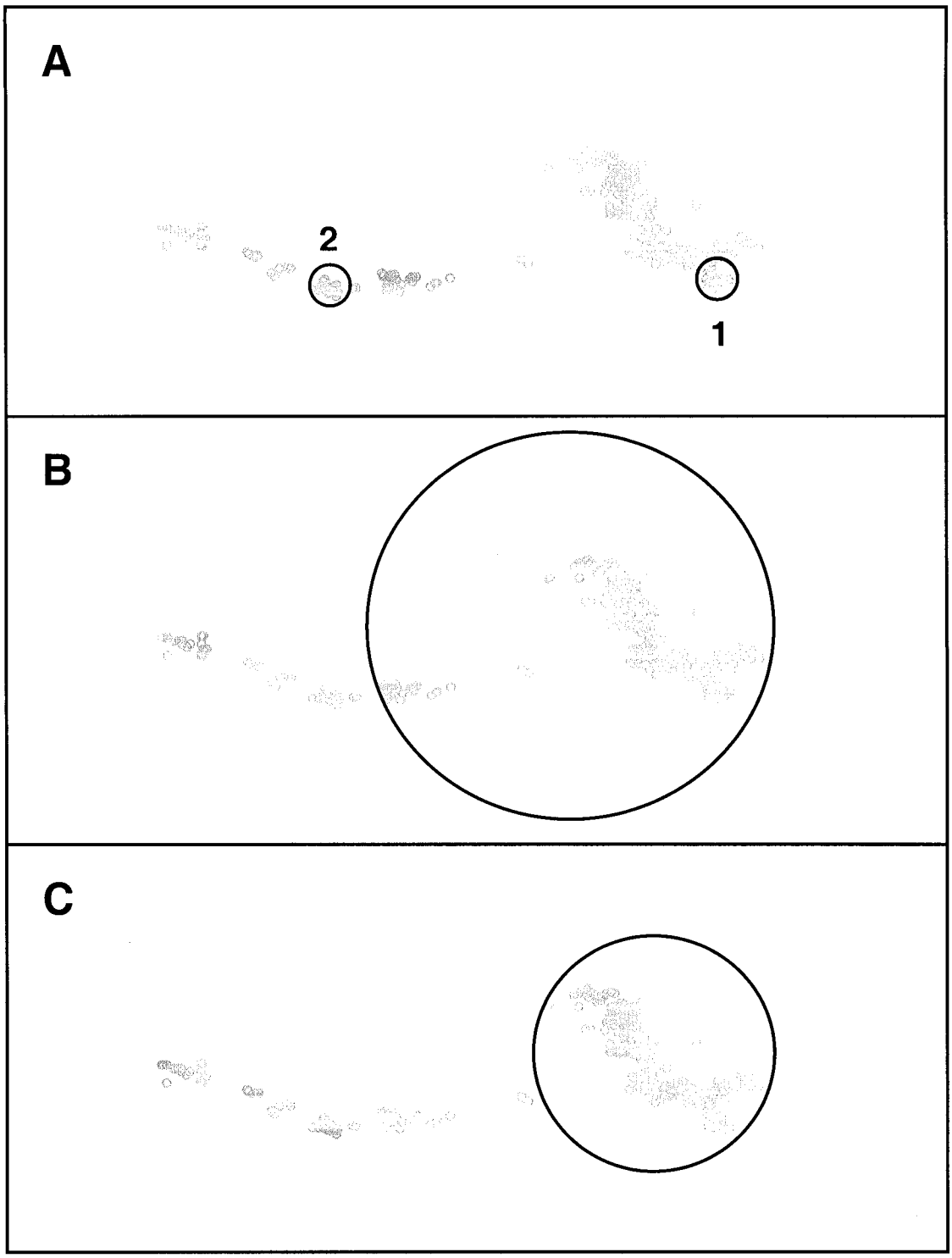

Figure 14. Selection of cluster parameter. Small gray circles designate locations of energy deposition events in an electron track end. A – cluster parameter is too small, B – cluster parameter is too large, C – cluster parameter is optimal.

cluster (panel C) and there is an optimal range of p for the entire population of electron tracks.

The optimal range of cluster parameters is not known *a priori*. The situation is similar to the classic K-means method, where desired number of clusters, K, has to be input into the algorithm. The basic technique to resolve this problem is described in detail in the Methods. The same approach is used here with respect to cluster parameter: a criterion that reflects "quality" of clusters is constructed and its behavior as a function of p is examined. The following *ad hoc* criterion is introduced:

$$C = \frac{order\ of\ the\ last\ cluster}{average\ cluster\ order} \tag{32}$$

In this formula, the numerator is the order of the last cluster in a table returned by the clustering algorithm. The denominator is the average of all cluster orders in the table.

The last cluster is used because it is considered to represent high-LET portion of an electron track in most cases. As an exercise to support this claim, 5-keV electron tracks generated by NOREC were processed with the clustering algorithm. For each track, all detected clusters were ranked as follows: the last cluster was assigned a rank of zero, the next-to-the-last cluster was given a rank of one, and so on. Then the largest cluster in a track (the cluster having maximal cluster order) was determined and its rank was recorded. The histograms of ranks based on 10,000 electron histories are presented in Fig. 15 for partitions with p = 0.03 μm and p = 0.05 μm. The choice of these values will become evident below. It is seen that the last cluster in a track is also the largest cluster most of the time (~60 % for p = 0.03 μm and ~70 % for p = 0.05 μm), the

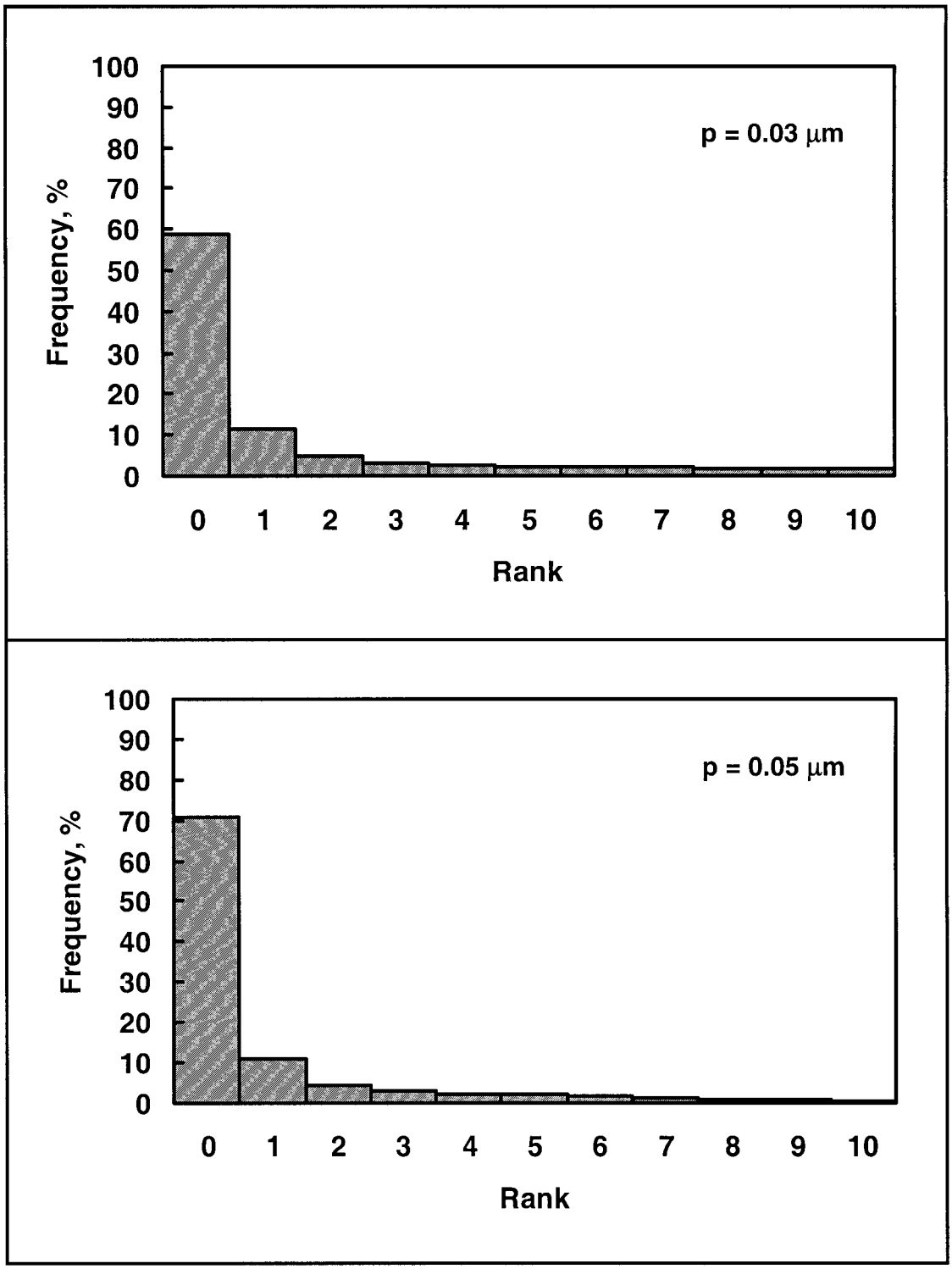

Figure 15. Data demonstrating that the last cluster is usually the largest cluster of the track.

remaining percentage accounting for cases when secondary electrons form clusters larger than the cluster formed at the end of the track of the primary electron.

It is important to develop an appropriate method for choosing p. If cluster parameter p is small (panel A in Fig. 14), the order of the last cluster would be not much different from the average of cluster orders and the ratio in equation 32 would be not much higher than unity. In the limiting case, when p is infinitesimally small, all "clusters" in a track will include only one event and the criterion becomes unity. If p is large (panel B), the difference in cluster order between the last cluster and the rest of clusters in a track is again diminished. In the limiting case of a very large p, only one cluster containing the entire track will be detected, which again gives $C = 1$. From these considerations, it is obvious that values of cluster parameter p that maximize the criterion in equation 32 would be considered optimal. The criterion was calculated for individual electron tracks and averaged over 200 electron histories used for each partition. The results are presented in Fig. 16 for a number of electron energies. It is concluded that the values of p between 0.03 μm and 0.05 μm should be used with the clustering algorithm. Ensuing analyses will be conducted using these boundary values and it will be demonstrated that the ultimate result, which is the fraction of energy deposited by high-LET events, is independent of the choice of cluster parameter p in this range.

Fig. 17 shows distributions of cluster order for the last cluster, representing the high-LET portion of an electron track, and the rest of clusters in the track, representing for the most part the low-LET portion. The histograms are obtained for three different electron energies (5,000 tracks each) using $p = 0.03$ μm. These distributions are fairly well separated so that one could establish a threshold value for cluster order that would

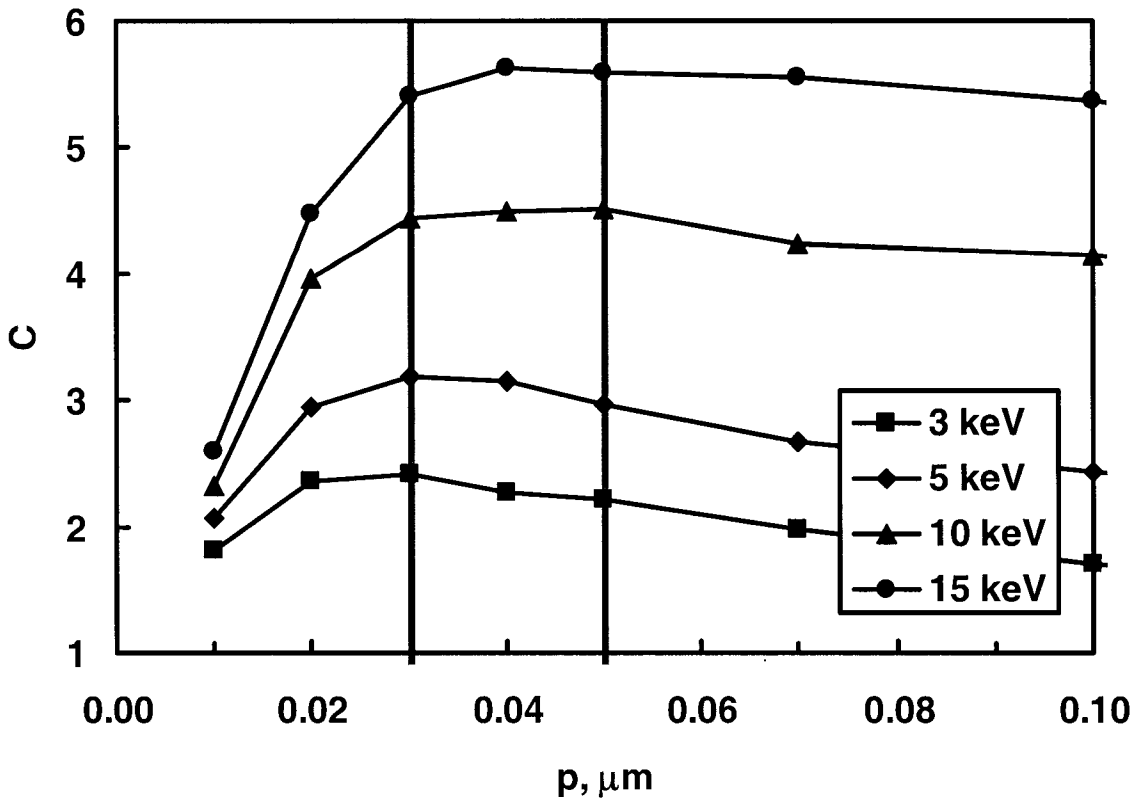

Figure 16. Cluster "quality" criterion as a function of cluster parameter. The optimal range for cluster parameter is indicated by reference lines.

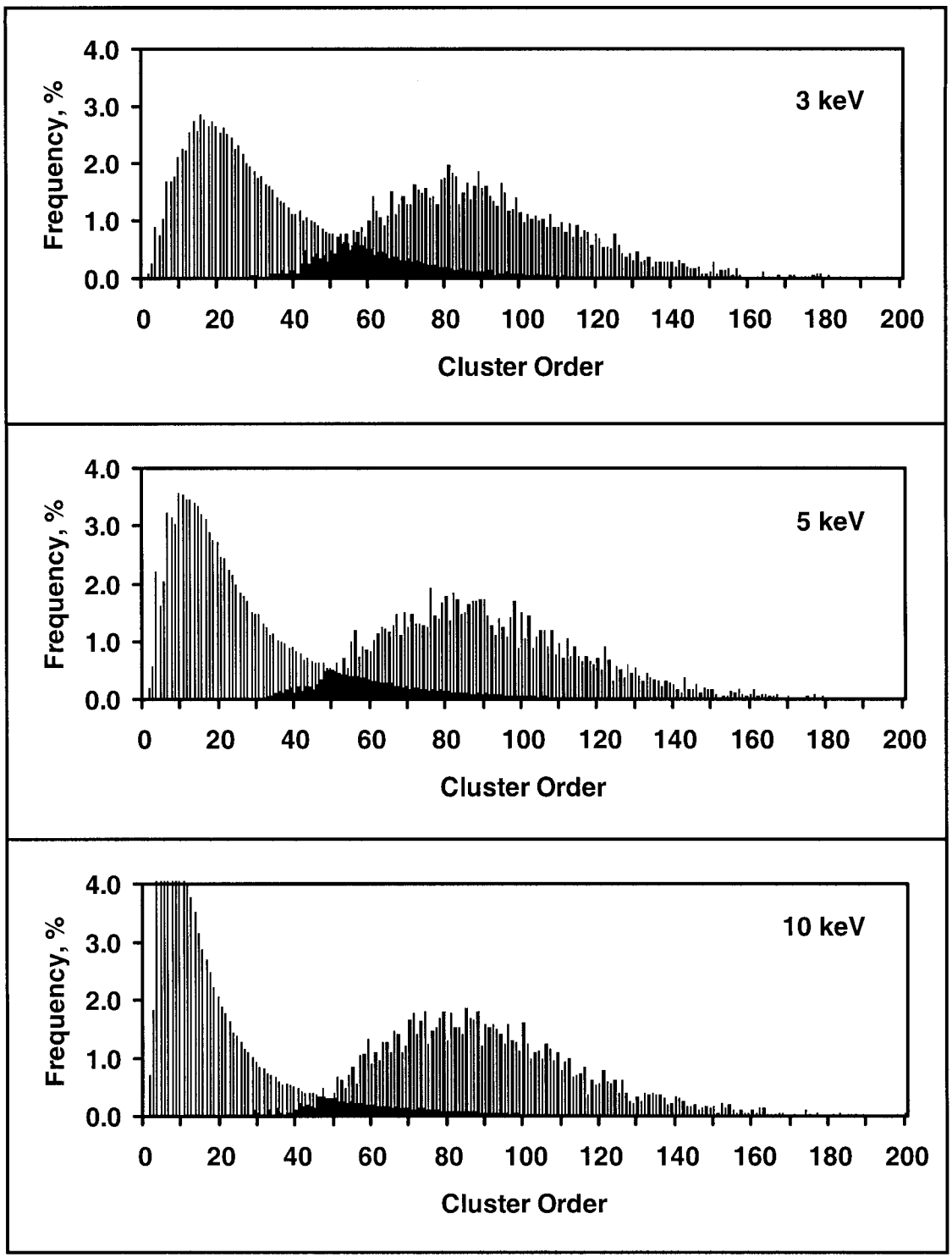

Figure 17. Distributions of cluster order for all-except-last clusters (left histograms) and for last clusters (right histograms). The data are for 5,000 electron tracks of three different initial electron energies partitioned using $p = 0.03$ μm.

discriminate between low-LET and high-LET clusters. It should be obvious that such threshold has to be independent of electron energy, since electrons have no "memory" of their initial energy, that is, the energy deposition pattern of, let's say, the residual 5 keV of a 10-keV track is statistically identical to the energy deposition pattern of an electron track with the initial energy of 5 keV. Therefore the decision about the threshold has to be made based solely on distributions for last clusters because 1) the distributions for all-except-last clusters on the left hand side of Fig. 17 include some clusters from energetic secondary electrons, which, in principle, pertain to high-LET part of electron tracks (such events are responsible for long right tails of those distributions); 2) the distributions for all-except-last clusters are energy dependent. In support of this claim, the data of Fig. 17 were rearranged to compare cumulative distributions of cluster order for all-except-last and last clusters by electron energy in Fig. 18. As expected, the distributions for last clusters are the same for all energies, whereas distributions for all-except-last clusters are different with the tendency toward more sparse clusters at higher electron energies. Such energy dependence also explains the behavior of the criterion C in Fig. 16: while the numerator in equation 32 is independent of energy, the denominator decreases as electron energy increases thus causing the curves for higher energies to be atop of the curves corresponding to lower energies.

The distributions of last cluster order for three different energies in Fig. 17 were pooled together and 1% quantile of the resulting distribution was taken to be the sought threshold value. This amounts to 46 energy deposition events for partitions with $p = 0.03$ μm. The data for $p = 0.05$ μm exhibits the same behavior and are not shown

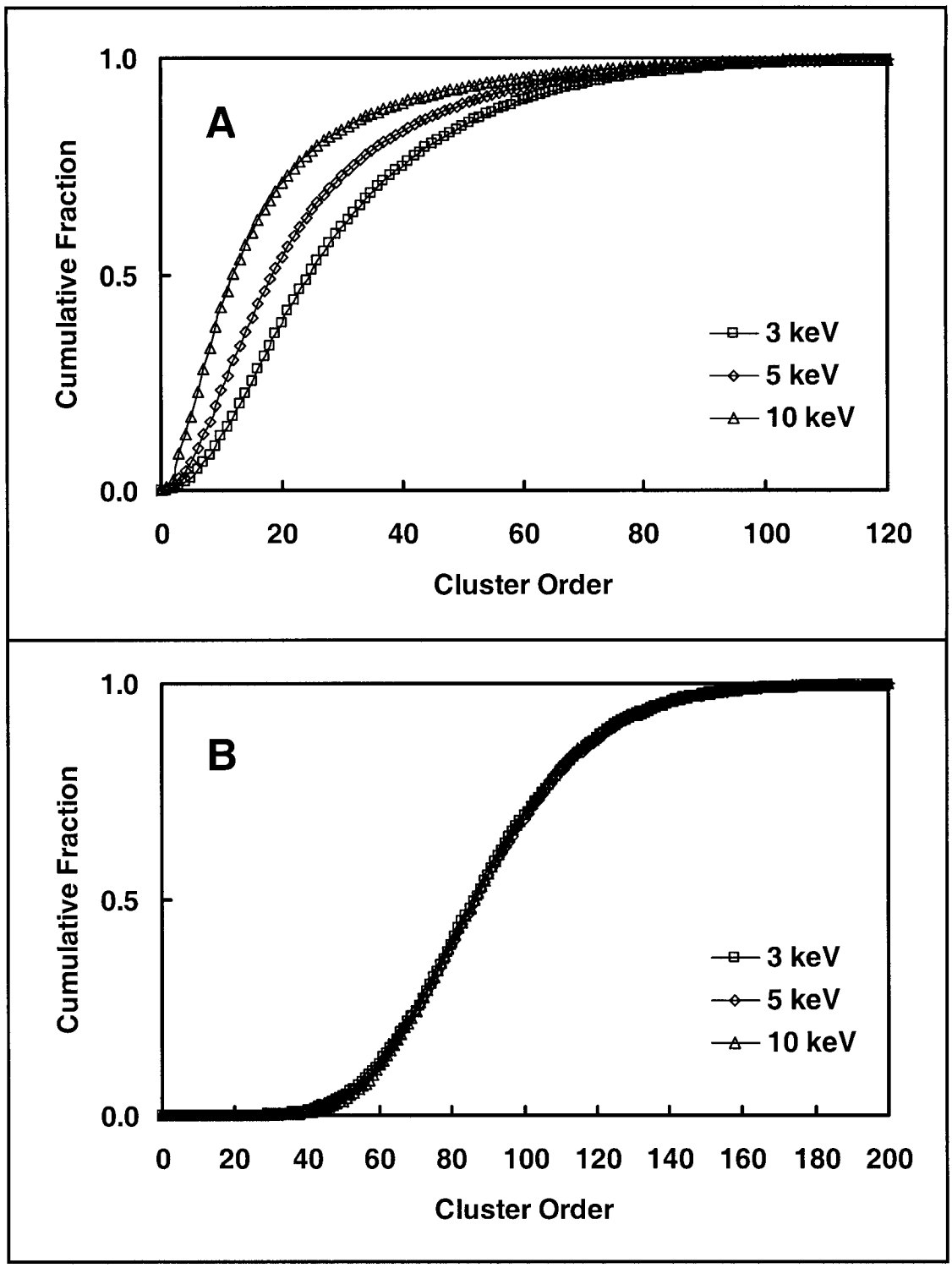

Figure 18. Cumulative distributions of cluster order for all-except-last clusters (A) and for last clusters (B) compared by electron energy. The data are the same as in Fig. 17.

here. In the same manner, the cluster order threshold for $p = 0.05$ μm was determined to be 70 energy deposition events.

Histograms of cluster order for last, high-LET clusters are presented in Fig. 19 for partitions with $p = 0.03$ μm and $p = 0.05$ μm along with reference lines showing the corresponding threshold values. From Fig. 19, it is concluded that high-LET clusters are formations containing from ~46 energy deposition events (the high-LET threshold for $p = 0.03$ μm) to up to 300 events (from the distribution for $p = 0.05$ μm). Taking into account high correlation between cluster order and cluster energy (Fig. 13), this translates into an approximate energy range of 360 eV – 2.4 keV.

Now that high-LET portion of electron tracks has been fully characterized, the next step is to apply the obtained definition to calculate the fraction of high-LET energy depositions for ^{3}H and ^{14}C. The scoring of energy deposition clusters was accomplished for single-track events only, that is, no clusters due to overlapping of multiple electron tracks were assumed. It was demonstrated earlier (*10*), that intertrack effects become significant only at extremely high doses. The calculation proceeds as follows:

1. Electron tracks generated with the Monte Carlo code NOREC are placed uniformly and isotropically inside a nucleus. Initial kinetic energies of electrons are sampled from the spectra of ^{3}H and ^{14}C.
2. Each electron history is followed, interaction-by-interaction, and energy deposition events that occur inside the nucleus are recorded in a table. As before, in case of ^{14}C, the follow-up is discontinued when electron escapes a 10-μm-thick shell around the nucleus. The entire electron histories are followed for ^{3}H.
3. The table generated in the previous step is processed with the clustering algorithm.

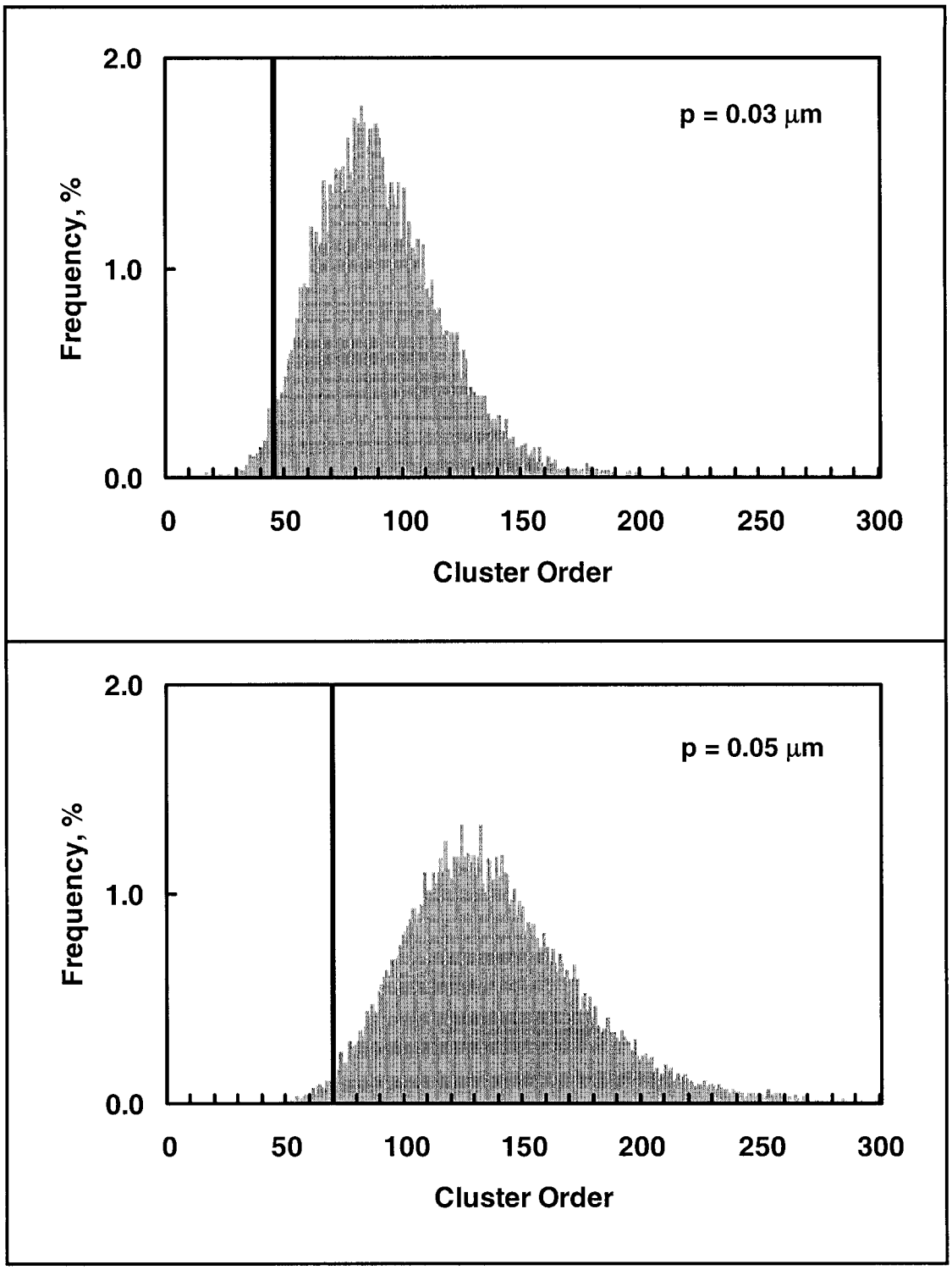

Figure 19. Distributions of cluster order for last clusters. High-LET thresholds for cluster order are shown by reference lines.

4. The output is scanned and, if a cluster order exceeds the threshold corresponding to the cluster parameter value used in partition, the energy deposited by such cluster is added to the portion of energy deposited by high-LET events, otherwise, it is added to low-LET portion of deposited energy.

5. The procedure is repeated for a large number of decays and the values of deposited energy are averaged.

6. The percent fraction of high-LET energy depositions is determined as

$$\varepsilon_{high-LET} = \frac{\overline{E}_{high-LET}}{\overline{E}_{low-LET} + \overline{E}_{high-LET}} \times 100\% \qquad (33)$$

The analysis was made for ^{3}H and ^{14}C inside cell nuclei described by the flat nucleus model using both p = 0.03 μm and p = 0.05 μm. The sum of low- and high-LET portions of energy in the denominator of equation 33 equals the average energy deposited in a nucleus. Values obtained in this calculation reproduced earlier results in Fig. 11. The fraction of energy deposited via high-LET events calculated by equation 33 is shown in Fig. 20 as a function of nucleus thickness. It is postulated that different values of cluster parameter within the range of 0.03 – 0.05 μm yield approximately the same estimate for the high-LET fraction of deposited energy providing that proper values of high-LET threshold for cluster order are selected.

It is concluded that the high-LET fraction is nearly independent of a cell nucleus configuration and amounts to ~30% for ^{14}C and ~43% for ^{3}H. This calculation shows that high-LET events do not constitute an absolute majority of energy deposition by tritium β particles as it was speculated in the beginning. On the other hand, the fraction

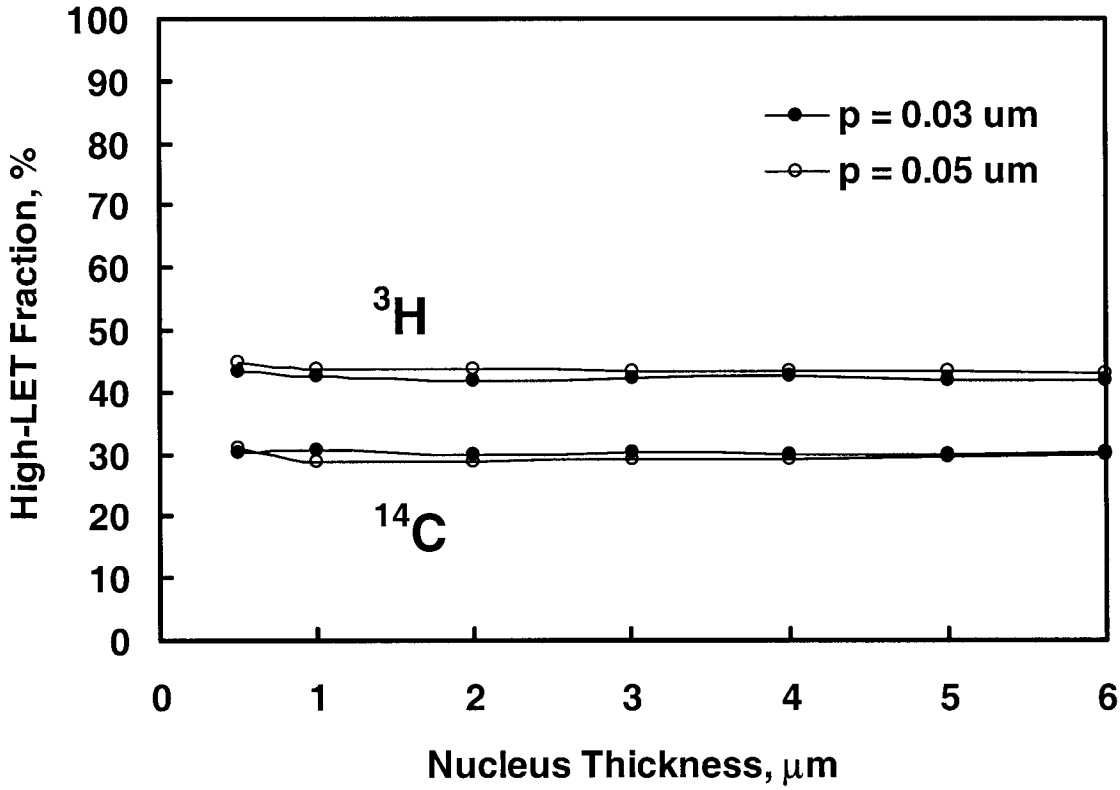

Figure 20. Percent high-LET fraction of deposited energy for ^{3}H and ^{14}C incorporated into cell nuclei described by the flat nucleus model. The data points are based on 5,000 beta decays each.

of high-LET energy deposition events in case of ^{14}C is higher than it was expected, which is attributed to considerable contribution from energetic secondary electrons that are capable of producing clusters at the ends of their tracks that are similar to the cluster at the end of the track of the primary electron.

Internuclear dose

The maximum CSDA range of tritium β particles, ~8 μm (Table 1), has the same order of magnitude as dimensions of a cell nucleus and that of ^{14}C β particles, ~300 μm, considerably exceeds these dimensions. Thus β particles of both radionuclides originating in nuclei of neighboring cells can potentially deposit energy in the nucleus of a target cell. It is important to estimate this contribution to the total dose absorbed in the target nucleus.

It is obvious that internuclear dose depends on the penetration capability of emitted radiation, the geometry of both target and source, and the distance between the two. In general, for a group of cells, one needs to know spatial distribution of all cells with corresponding distances and nuclear sizes. The following assumptions about these parameters have been made:

1) the flat nucleus model is used to describe cell nuclei;

2) cells are assumed to be ellipsoids with axes that are three times larger than the axes of corresponding nuclei;

3) small ellipsoids (cell nuclei) and large ellipsoids (cells) are concentric;

4) cells are positioned in a monolayer honeycomb-like structure so that cytoplasmic membranes of adjacent cells touch each other (Fig. 21).

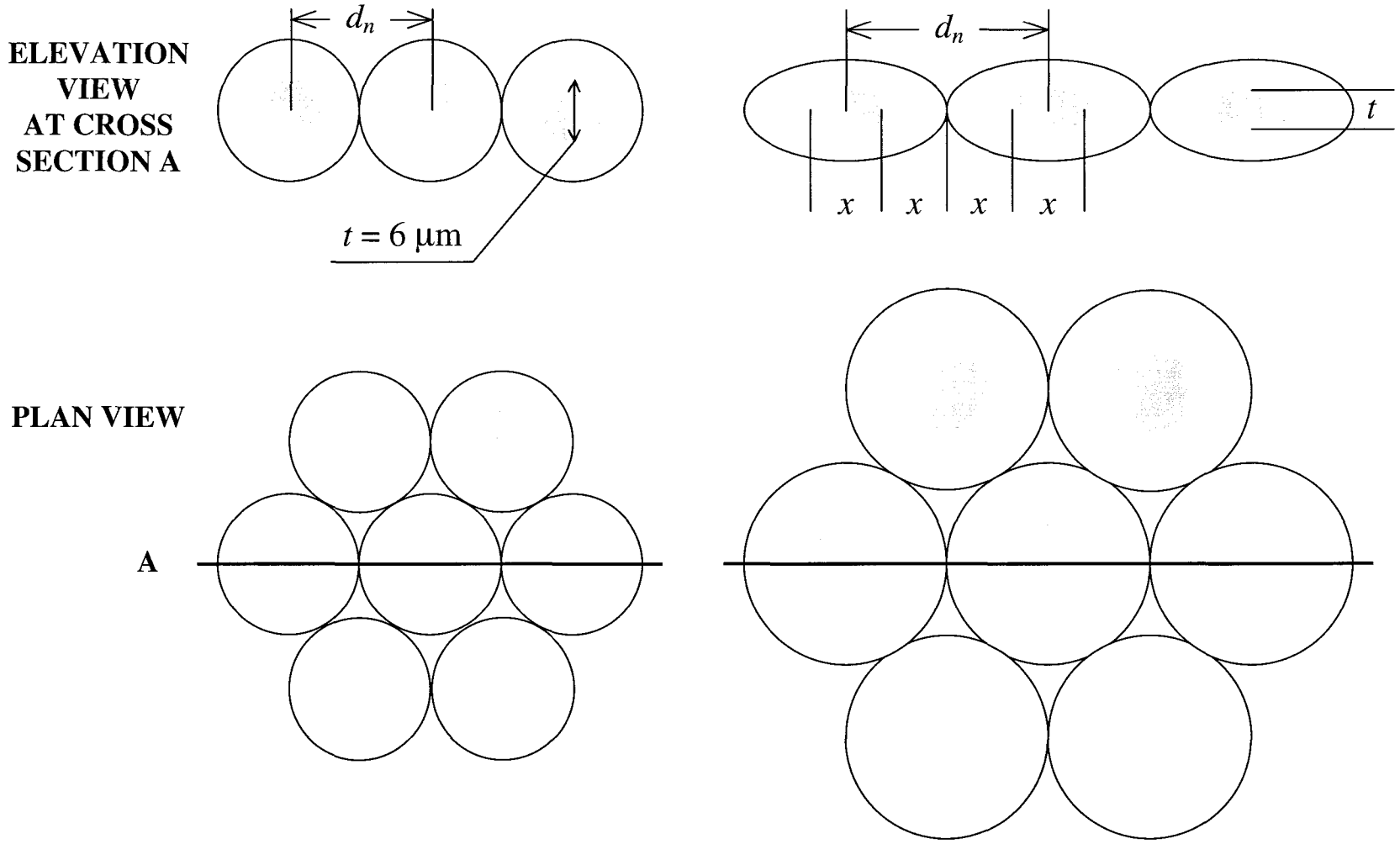

Figure 21. Multi-cell model. Gray areas are cell nuclei. The model is a function of nucleus thickness, $0 < t \leq 6$ µm.

It is also assumed that penetration of electrons through nucleus, cytoplasm and intercellular medium is satisfactory approximated by electron transport in bulk water. The distance between centers of nuclei, d_n, varies with nuclear thickness, t, and can be determined as

$$d_n(t) = 3 \cdot x(t) = 3 \cdot \sqrt{\frac{3^3 \cdot 8}{t}} \ , \tag{34}$$

where $x(t)$ is given by equation 30.

Spherical nuclei (t = 6 μm) are the closest ones with d_n = 18 μm. The distance between the surfaces of nuclei in this case is 12 μm, which is larger than the CSDA range of the most energetic electrons in the spectrum of ^{3}H, ~8 μm. Therefore under the current assumptions, tritium β particles are incapable of reaching even the nuclei of adjacent cells and internuclear dose is of no concern.

Further analysis will thus be focused on internuclear dose for ^{14}C. Consider the following calculation. Cells, numbered from zero to three, are aligned in a row so that their cytoplasmic membranes touch. Cellular and nuclear geometries are specified by the above-described model. ^{14}C is distributed uniformly in the nucleus of the cell with number zero, which hereafter will be referred to as zero nucleus. Energy deposited in all nuclei is computed by following entire NOREC electron histories with initial energies from ^{14}C spectrum. To improve statistics, rows of cells one through three were placed in four perpendicular directions around the zero cell and resulting energies were averaged. The average energy deposited in the nuclei of cells one through three, expressed as a percentage of energy deposited in the zero nucleus are shown in Fig. 22 for different

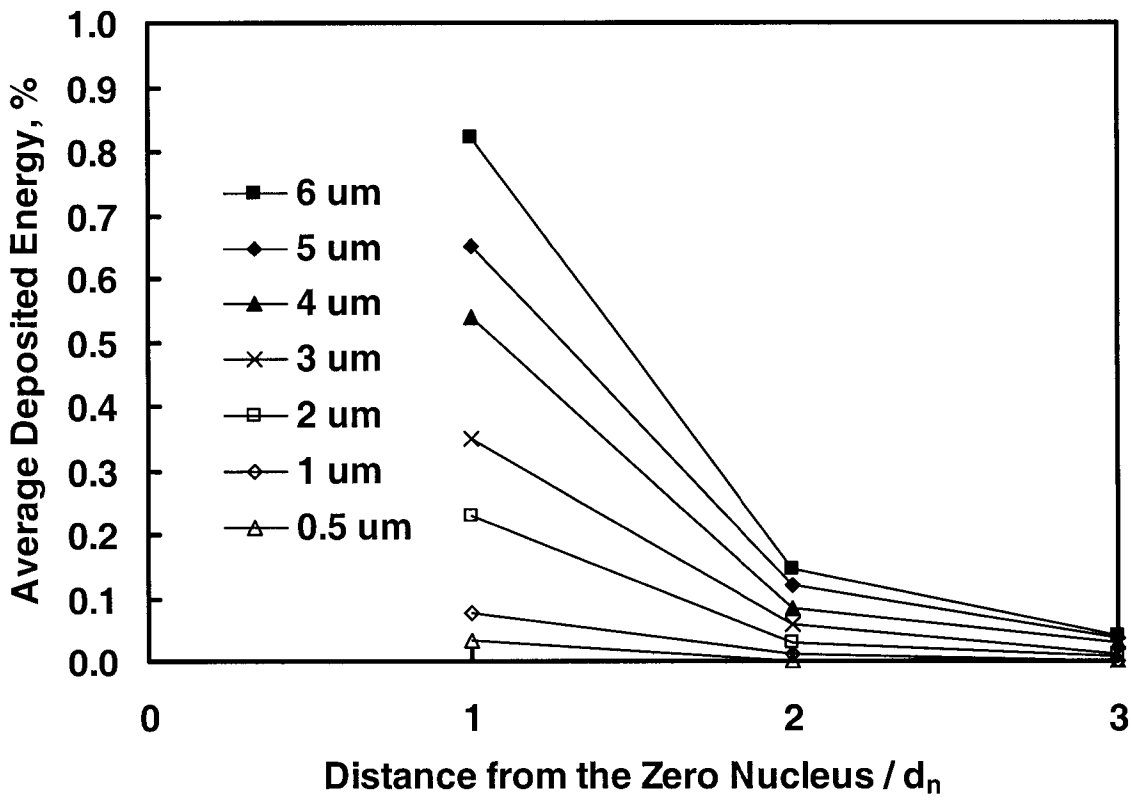

Figure 22. Average energy deposited in nuclei of neighboring cells per disintegration occurring in the nucleus of the cell nucleus containing uniformly distributed source of ^{14}C (zero nucleus). The deposited energy is expressed as a percentage of the average energy deposited in the zero nucleus. Calculations are made for different geometries specified by the flat nucleus model (nucleus thickness is given in the legend). The results are based on 100,000 beta decays in the zero nucleus for each geometry.

geometries. These results demonstrate a quick fall of energy deposited in neighboring nuclei as they are distanced from the zero nucleus. Although the most energetic β particles in ^{14}C spectrum with the CSDA range of ~300 μm could theoretically reach as far as sixteenth cell nucleus in a row of spherical cells (t = 6 μm), the amount of energy deposited in nuclei of cells beyond the third cell in a row is very small (below 0.05% of energy deposition in the zero nucleus for any geometry) and thus can be neglected.

Hence, only nuclei of cells in the configuration depicted in Fig. 23 are considered to receive appreciable amount of energy from a ^{14}C source located in the zero nucleus. Let us calculate the total energy that would be deposited in such structure. The distance between centers of cells labeled 0 and A is $\sqrt{3}d_n$ and that between centers of cells 0 and B is $\sqrt{7}d_n$. Energy deposited in nuclei of cells A and B can be roughly estimated from Fig. 22 by linear interpolation, as ordinate values at 1.732 and 2.646 respectively. Summing deposited energy for nuclei of all cells surrounding the zero cell in Fig. 23, one obtains the plot in Fig. 24. By reciprocity, the average energy that ^{14}C source distributed in the zero nucleus deposits in nuclei of surrounding cells equals the average energy that would be deposited in the zero nucleus by similar sources in nuclei of neighboring cells. The dependence in Fig. 24 is thus the average internuclear dose to a cell nucleus due to ^{14}C expressed as a percentage of the intranuclear dose. These results applied to the curve of intranuclear dose (Fig. 12) are shown in Fig. 25. Thus the internuclear component of absorbed dose for ^{14}C is the largest for spherical nuclei and decreases as nuclei become more and more flat. It should be realized that the current estimate of internuclear dose depends to a great extent on the adopted assumptions about sizes and proximity of cell nuclei.

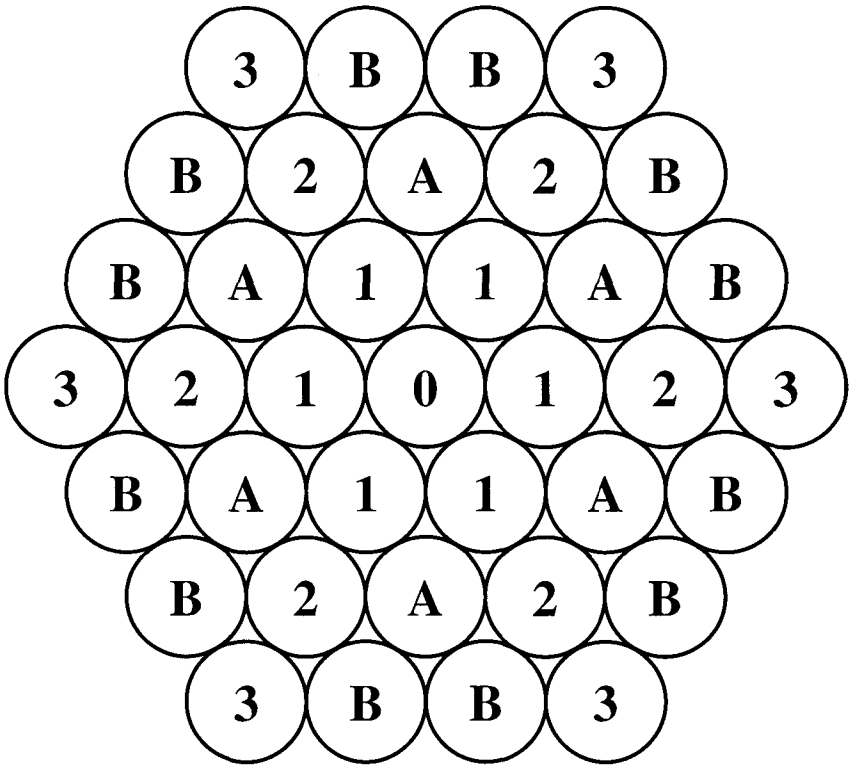

Figure 23. Cells that would have significant amount of energy deposited in their nuclei by ^{14}C source uniformly distributed in the nucleus of the cell labeled zero.

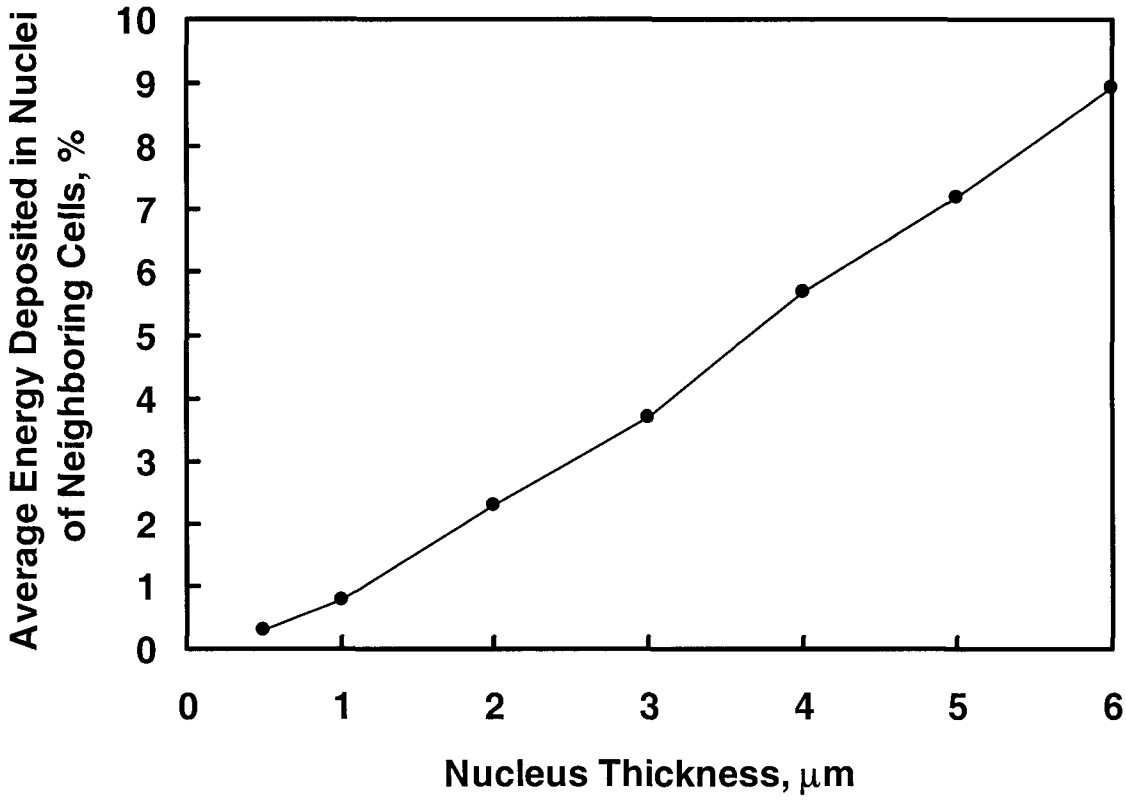

Figure 24. Average energy deposited in nuclei of cells surrounding the zero cell expressed as a percentage of the average energy deposited in the zero nucleus.

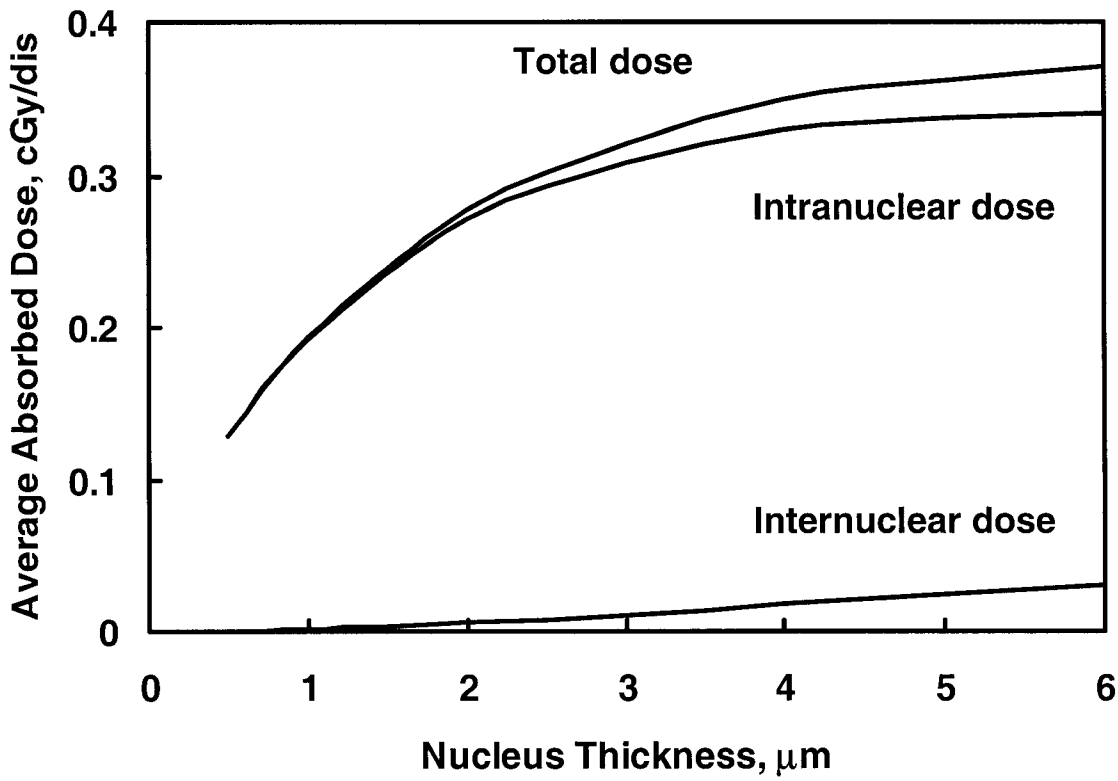

Figure 25. Intranuclear versus internuclear dose for ^{14}C uniformly distributed in cell nuclei described by the flat nucleus model.

The question remains for ^{14}C whether the fraction of high-LET energy depositions is larger for internuclear dose, which could affect the overall value of high-LET fraction (due to both intranuclear and internuclear dose). Calculation of this fraction for the energy deposited in the 6-μm-diameter zero nucleus by β particles originating in nuclei of adjacent cells (cells labeled 1 according to the terminology above) indicated the value of approximately 26%. This is actually smaller than the high-LET fraction for the intranuclear dose, 30%. The explanation for this result could be that the internuclear dose is deposited in this case by intermediate segments of electron tracks (predominantly low-LET) rather than the terminal part. All in all, since the internuclear dose is only a few percent of the intranuclear dose, the overall high-LET fraction for ^{14}C would not differ considerably from the estimate for the intranuclear dose, about 30%.

CHAPTER 5. CONCLUSIONS

This research is focused on investigating energy deposition characteristics of ^{3}H and ^{14}C uniformly incorporated into the nucleus of a cell. Dosimetric estimates were obtained by means of simulating beta decay of ^{3}H and ^{14}C and energy deposition processes by electrons in water. The latter was achieved by using Monte Carlo electron track-structure codes. Three Monte Carlo codes developed by different scientific groups were compared with respect to the average energy deposited by ^{3}H and ^{14}C in micrometer-sized spherical volumes representing cell nuclei. Two of the codes were created for liquid water and one was for water vapor. Results produced by all the codes were in close agreement. This is consistent with conclusions of previous works aimed at comparing different track-structure codes for gaseous and liquid water (*45, 73, 74*). The basic findings of such comparisons are that the results are rather similar for larger targets, such as nucleosomes and chromatin (diameter of ~10 – 25 nm), and differences begin to appear at the smaller scales, such as for DNA (diameter of ~2 nm). Dosimetric methods employing electron tracks simulated with Monte Carlo computer codes are computationally more challenging, but are considered to yield more credible results than traditionally used analytical methods for dosimetry of ^{3}H and ^{14}C in a cell nucleus.

Calculations of intranuclear and internuclear dose were performed using geometrical models of a cell nucleus. These models are functions of some parameter (e.g., radius for the spherical nucleus model or thickness for the flat nucleus model).

Such approach provides a broader understanding of behavior of absorbed dose. The internuclear dose was estimated to be negligible for ^{3}H and that for ^{14}C was determined to be a few percent the intranuclear dose. The latter estimate is based largely on adopted assumptions about spatial distribution of nuclei and nuclear sizes. Once results of measurements of these parameters are available for the final choice of cells and treatments to be used in the experiment, the developed methodology can be readily applied to obtain specific dose estimates.

Clustering techniques were used to characterize electron track ends and determine the fraction of high-LET energy deposition events in the spectra of ^{3}H and ^{14}C. Track-end clusters were described as entities having dimensions of 0.03 – 0.05 μm and capable of depositing energy from ~360 eV to a few keV. The fraction of absorbed dose due to such events was determined to be about 43% for ^{3}H and about 30% for ^{14}C. These values appear to be independent of geometry for a cell nucleus. The determined percentages are compatible with earlier estimates of the fraction of energy (or dose) deposited by all low-LET radiations via low-energy electrons, ~30-50% (see Literature Review).

Low-energy electrons similar to those responsible for track-end clusters are created by all radiations, either directly or through interaction with matter. Criteria developed in this work to determine frequencies of such events are universal in a sense that they can be applied to a spectrum of electrons produced by any other radiation.

REFERENCES

1. D. T. Goodhead, J. Thacker and R. Cox, Effectiveness of 0.3 keV carbon ultrasoft X-rays for the inactivation and mutation of cultured mammalian cells. *Int. J. Radiat. Biol.* **36**, 101-114 (1979).

2. R. P. Virsik, C. Schäfer, D. Harder, D. T. Goodhead, R. Cox and J. Thacker, Chromosome aberrations induced in human lymphocytes by ultrasoft Al_K and C_K X-rays. *Int. J. Radiat. Biol.* **38**, 545-557 (1980).

3. D. Frankenberg, D. T. Goodhead, M. Frankenberg-Schwager, R. Harbich, D. A. Bance and R. E. Wilkinson, Effectiveness of 1.5 keV aluminum K and 0.3 keV carbon K characteristic X-rays at inducing DNA double-strand breaks in yeast cells. *Int. J. Radiat. Biol.* **50**, 727-741 (1986).

4. M. R. Raju, S. G. Carpenter, J. J. Chmielewski, M. E. Schillaci, M. E. Wilder, J. P. Freyer, N. F. Johnson, P. L. Schor, R. J. Sebring and D. T. Goodhead, Radiobiology of ultrasoft X rays. I. Cultured hamster cells (V79). *Radiat. Res.* **110**, 396-412 (1987).

5. D. J. Brenner, R. P. Bird, M. Zaider, P. Goldhagen, P. J. Kliauga and H. H. Rossi, Inactivation of synchronized mammalian cells with low-energy X rays – results and significance. *Radiat. Res.* **110**, 413-427 (1987).

6. K. M. Prise, M. Folkard, S. Davies and B. D. Michael, Measurements of DNA damage and cell killing breaks in Chinese hamster V79-4 cells irradiated with aluminum characteristic ultrasoft X rays. *Radiat. Res.* **117**, 489-499 (1989).

7. D. Frankenberg, H. Kühn, M. Frankenberg-Schwager, W. Lenhard and S. Beckonert, 0.3 keV carbon K ultrasoft X-rays are four times more effective than γ-rays when inducing oncogenic cell transformation at low doses. *Int. J. Radiat. Biol.* **68**, 593-601 (1995).

8. S. W. Botchway, D. L. Stevens, M. A. Hill, T. J. Jenner and P. O'Neill, Induction and rejoining of DNA double-strand breaks in Chinese hamster V79-4 cells irradiated with characteristic aluminum K and copper L ultrasoft X rays. *Radiat. Res.* **148**, 317-324 (1997).

9. C. M. de Lara, M. A. Hill, T. J. Jenner, D. Papworth and P. O'Neill, Dependence of the yield of DNA double-strand breaks in Chinese hamster V79-4 cells on the photon energy of ultrasoft X rays. *Radiat. Res.* **155**, 440-448 (2001).

10. D. T. Goodhead and H. Nikjoo, Track structure analysis of ultrasoft X-rays compared to high- and low-LET radiations. *Int. J. Radiat. Biol.* **55**, 513-529 (1989).

11. H. Nikjoo and D. T. Goodhead, Track structure analysis illustrating the prominent role of low-energy electrons in radiobiological effects of low-LET radiations. *Phys. Med. Biol.* **36**, 229-238 (1991).

12. M. E. Schillaci, S. G. Carpenter, M. R. Raju, R. J. Sebring, M. E. Wilder and D. T. Goodhead, Radiobiology of ultrasoft X rays. II. Cultured C3H mouse cells (10T½). *Radiat. Res.* **118**, 83-92 (1989).

13. M. N. Cornforth, M. E. Schillaci, D. T. Goodhead, S. G. Carpenter, M. E. Wilder, R. J. Sebring and M. R. Raju, Radiobiology of ultrasoft X rays. III. Normal human fibroblasts and the significance of terminal track structure in cell inactivation. *Radiat. Res.* **119**, 511-522 (1989).

14. C. K. Hill, B. E. Nelms, J. F. MacKay, D. W. Pearson, W. S. Kennan, T. R. Mackie, P. M. DeLuca, Jr., M. J. Lindstrom and M. N. Gould, Synchrotron-produced ultrasoft X rays: equivalent cell survival at the isoattenuation energies 273 eV and 860 eV. *Radiat. Res.* **150**, 513-520 (1998).

15. K. Tägder and W. Scheuermann, Estimation of absorbed doses in the cell nucleus after incorporation of ^{3}H- or ^{14}C-labeled thymidine. *Radiat. Res.* **41**, 202-216 (1970).

16. A. Shiragai, Comment on estimation methods of absorbed dose due to tritium. *J. Radiat. Res.* **12**, 73-86 (1971).

17. J. S. Nettleton and R. S. Lawson, Cellular dosimetry of diagnostic radionuclides for spherical and ellipsoidal geometry. *Phys. Med. Biol.* **41**, 1845-1854 (1996).

18. H. H. Rossi and R. H. Ellis, Distributed beta sources in uniformly absorbing media–I. *Nucleonics* **7**, 18-25 (1950).

19. T. H. Oddie, Dosage from radioisotopes uniformly distributed within a sphere. *Brit. J. Radiol.* **24**, 333-336 (1951).

20. R. Loevinger, The dosimetry of beta sources in tissue. The point-source function. *Radiology* **66**, 55-62 (1956).

21. J. S. Robertson and W. L. Hughes, Theoretic considerations of the radiation dose from discrete tritium sources, *Radiology* **68**, 102 (1957).

22. J. S. Robertson and W. L. Hughes, Intranuclear irradiation with tritium-labeled thymidine, In *Proc. of the 1st National Biophysics Conference* (H. Quastler and H. J. Morowitz, Eds.), pp. 278-283. Yale University Press, New Haven (1959).

23. J. S. Robertson, V. P. Bond and E. P. Cronkite, Resolution and image spread in autoradiographs of tritium-labeled cells, *Int. J. Appl. Rad. Isotopes* **7**, 33-37 (1959).

24. C. R. Goodheart, Radiation dose calculation in cells containing intranuclear tritium. *Radiat. Res.* **15**, 767-773 (1961).

25. F. S. Stewart, The calculation of radiation dose from distributed sources of tritium. *Int. J. Radiat. Biol.* **8**, 545-549 (1964).

26. H. A. Künkel, Zur Frage der Strahlenbelastung des Zellkerns durch Inkorporation von tritium-markiertem Thymidin. *Strahlentherapie* **118**, 46-53 (1962).

27. M. J. Berger, Beta-ray dosimetry calculations with the use of point kernels. In *Medical radionuclides: radiation dose and effects*, (R. J. Cloutier, C. L. Edwards and W. S. Snyder, Eds.), pp. 63-86. U.S. Atomic Energy Commission (1970).

28. M. J. Berger, Distribution of absorbed dose around point sources of electrons and beta particles in water and other media. *J. Nucl. Medicine*, Suppl. **5**, 5-23 (1971).

29. A. Shiragai, Futher comments on estimation methods of absorbed doses due to tritium. *J. Radiat. Res.* **13**, 208-213 (1972).

30. E. J. Kobetich and R. Katz, Electron energy dissipation. *Nucl. Instr. and Meth.* **71**, 226-230 (1969).

31. S. M. Goddu, R. W. Howell and D. V. Rao, Cellular dosimetry: absorbed fractions for monoenergetic electron and alpha particle sources and S-values for radionuclides uniformly distributed in different cell compartments. *J. Nucl. Med.* **35**, 303-316 (1994).

32. S. Apelgot and M. Duquesne, Énergie dissipée par le tritium dans des microorganisms. *Int. J. Radiat. Biol.* **7**, 65-74 (1963).

33. W. Künh, Methode zur Berechnung der Dosis bei inkorporierten Beta-Strahlen in annähernd symmetrischen Microbereichen. *Biophysik* **4**, 187-195 (1968).

34. D. T. Goodhead, The initial physical damage produced by ionizing radiations. *Int. J. Radiat. Biol.* **56**, 623-634 (1989).

35. H. Nikjoo S. Uehara, W. E. Wilson, M. Hoshi and D. T. Goodhead, Track structure in radiation biology: theory and applications. *Int. J. Radiat. Biol.* **73**, 355-364 (1998).

36. V. Michalik, Particle track structure and its correlation with radiobiological endpoint. *Phys. Med. Biol.* **36**, 1001-1012 (1991).

37. V. Michalik, Energy deposition clusters in nanometer regions of charged-particle tracks. *Radiat. Res.* **134**, 265-270 (1993).

38. D. J. Brenner and J. F. Ward, Constraints on energy deposition and target size of multiply damaged sites associated with DNA double-strand breaks. *Int. J. Radiat. Biol.* **61**, 737-748 (1992).

39. V. V. Moiseenko, A. A. Edwards, H. Nikjoo and W. V. Prestwich, The influence of track structure on the understanding of relative biological effectiveness for induction of chromosomal exchanges in human lymphocytes. *Radiat. Res.* **147**, 208-214 (1997).

40. V. V. Moiseenko, A. J. Waker and W. V. Prestwich, Energy deposition pattern from tritium and different energy photons – a comparative study. *Health Phys.* **73**, 388-392 (1997).

41. S. M. Goddu, D. V. Rao and R. W. Howell, Multicellular dosimetry for micrometastases: dependence of self-dose versus cross-dose to cell nuclei on type and energy of radiation and subcellular distribution of radionuclides. *J. Nucl. Med.* **35**, 521-530 (1994).

42. M. R. Raju, Y. Eisen, S. Carpenter and W. C. Inkret, Radiobiology of α particles. III. Cell inactivation by α-particle traversals of the cell nucleus. *Radiat. Res.* **128**, 204-209 (1991).

43. ICRU, *Dosimetry of external beta rays for radiation protection.* Report 56, International Commission on Radiation Units and Measurements, Bethesda, MD, 1997.

44. W. H. Press, S. A. Teukolsky, W. T. Vetterling and B. P. Flannery, *Numerical recipes in C: the art of scientific computing*, 2nd ed. Cambridge University Press, New York, 1992.

45. S. Uehara, H. Nikjoo and D. T. Goodhead, Comparison and assessment of electron cross sections for Monte Carlo track structure codes. *Radiat. Res.* **152**, 202-213 (1999).

46. R. N. Hamm, H. A. Wright, R. H. Ritchie, J. E. Turner and T. P. Turner, Monte Carlo calculation of transport of electrons through liquid water. In *Proceedings of the Fifth Symposium on Microdosimetry, Verbania-Pallanza* (J. Booz, H. G. Ebert and B. G. R. Smith, Eds.), Vol. II, pp. 1037-1053. Commission of the European Communities, Brussels, 1976.

47. R. H. Ritchie, R. N. Hamm, J. E. Turner and H. A. Wright, The interaction of swift electrons with liquid water. In *Sixth Symposium on Microdosimetry, Brussels, Belgium* (J. Booz and H. G. Ebert, Eds.), Vol. I, pp. 345-354. Commission of the European Communities, Harwood, London, 1978.

48. R. H. Ritchie, R. N. Hamm, J. E. Turner, H. A. Wright and W. E. Bolch, Radiation interactions and energy transport in the condensed phase. In *Physical and Chemical Mechanisms in Molecular Radiation Biology* (W. A. Glass and M. N. Varma, Eds.), pp. 99-135. Plenum Press, New York, 1991.

49. J. E. Turner, J. L. Magee, H. A. Wright, A. Chatterjee, R. N. Hamm and R. H. Ritchie, Physical and chemical development of electron tracks in liquid water. *Radiat. Res.* **96**, 437-449 (1983).

50. J. E. Turner, R. N. Hamm, H. A. Wright, R. H. Ritchie, J. L. Magee, A. Chatterjee and W. E. Bolch, Studies to link the basic radiation physics and chemistry of liquid water. *Radiat. Phys. Chem.* **32**, 503-510 (1988).

51. W. E. Bolch, J. E. Turner, H. Yoshida, K. B. Jacobson, H. A. Wright and R. N. Hamm, Monte Carlo calculations of free ammonia production in deoxygenated solutions of glycylglycine irradiated by X rays and ^{60}Co gamma rays. *Radiat. Res.* **121**, 248-256 (1990).

52. J. E. Turner, W. E. Bolch, H. Yoshida, K. B. Jacobson, H. A. Wright, R. N. Hamm, R. H. Ritchie and C. E. Klots, Radiation damage to a biomolecule: new physical model successfully traces molecular events. *Int. J. Rad. Appl. Instrum. Part A* **42**, 995-1001 (1991).

53. J. E. Turner, R. N. Hamm, R. H. Ritchie and W. E. Bolch, Monte Carlo track-structure calculations for aqueous solutions containing biomolecules. In *Computational Approaches in Molecular Radiation Biology. Monte Carlo Methods* (M. N. Varma and A. Chatterjee, Eds.), pp. 155-166. Plenum Press, New York, 1994.

54. W. E. Bolch, J. E. Turner, H. Yoshida, K. B. Jacobson, R. N. Hamm and O. H. Crawford, Product yields from irradiated glycylglycine in oxygen-free solutions: Monte Carlo simulations and comparison with experiments. *Radiat. Environ. Biophys.* **37**, 157-166 (1998).

55. R. N. Hamm, M. G. Stabin and J. E. Turner, Investigation of a Monte Carlo model for chemical reactions. *Radiat. Environ. Biophys.* **37**, 151-156 (1998).

56. B. Aydogan, D. T. Marshall, S. G. Swarts, J. E. Turner, A. J. Boone, N. G. Richards and W. E. Bolch, Site-specific OH attack to the sugar moiety of DNA: a comparison of experimental data and computational simulation. *Radiat. Res.* **157**, 38–44 (2002).

57. H. A. Wright, J. L. Magee, R. N. Hamm, A. Chatterjee, J. E. Turner and C. E. Klots, Calculations of physical and chemical reactions produced in irradiated water containing DNA. *Radiat. Prot. Dosim.* **13**, 133-136 (1985).

58. H. A. Wright, R. N. Hamm, J. E. Turner, R. W. Howell, D. V. Rao and K. S. R. Sastry, Calculations of physical and chemical reactions with DNA in aqueous solutions from Auger cascades. *Radiat. Prot. Dosim.* **31**, 59-62 (1990).

59. V. V. Moiseenko, R. N. Hamm, A. J. Waker and W. V. Prestwich, Modelling DNA damage induced by different energy photons and tritium beta-particles. *Int. J. Radiat. Biol.* **74**, 533-550 (1998).

60. V. V. Moiseenko, R. N. Hamm, A. J. Waker and W. V. Prestwich, The cellular environment in computer simulations of radiation-induced damage to DNA. *Radiat. Environ. Biophys.* **37**, 167-172 (1998).

61. V. V. Moiseenko, R. N. Hamm, A. J. Waker and W. V. Prestwich, Calculation of radiation-induced DNA damage from photons and tritium beta-particles. Part I: Model formulation and basic results. *Radiat. Environ. Biophys.* **40**, 23-31 (2001).

62. V. V. Moiseenko, R. N. Hamm, A. J. Waker and W. V. Prestwich, Calculation of radiation-induced DNA damage from photons and tritium beta-particles. Part II: Tritium RBE and damage complexity. *Radiat. Environ. Biophys.* **40**, 33-38 (2001).

63. J. E. Turner, R. N. Hamm, M. L. Souleyrette, D. E. Martz, T. A. Rhea and D. W. Schmidt, Calculations for β dosimetry using Monte Carlo code (OREC) for electron transport in water. *Health Phys.* **55**, 741-750 (1988).

64. O. H. Crawford, J. E. Turner, R. N. Hamm and J. C. Ashley, Effects of the tissue-air interface in calculations of β-particle skin dose at a depth of 70 μm. *Health Phys.* **61**, 641-645 (1991).

65. W. Friedland, P. Jacob, H. G. Paretzke and T. Stork, Monte Carlo simulation of the production of short DNA fragments by low-linear energy transfer radiation using higher-order DNA models. *Radiat. Res.* **150**, 170-182 (1998).

66. M. Dingfelder, D. Hantke, M. Inokuti and H. G. Paretzke, Electron inelastic-scattering cross sections in liquid water. *Radiat. Phys. Chem.* **53**, 1-18 (1998).

67. S. Uehara, H. Nikjoo and D. T. Goodhead, Cross-sections for water vapour for the Monte Carlo electron track structure code from 10 eV to the MeV region. *Phys. Med. Biol.* **37**, 1841-1858 (1992).

68. J. A. Hartigan, *Clustering Algorithms*, John Wiley & Sons, Inc., New York, 1975.

69. J. A. Hartigan and M. A. Wong, Algorithm AS 136: a K-means clustering algorithm. *Appl. Stat.* **28**, 100-108 (1979).

70. H. Späth, *Cluster analysis algorithms for data reduction and classification of objects*, Halsted Press, New York, 1980.

71. G. W. Milligan and M. C. Cooper, An examination of procedures for determining the number of clusters in a data set. *Psychometrika* **50**, 159-179 (1985).

72. A. M. Kellerer, Chord-length distributions and related quantities for spheroids. *Radiat. Res.* **98**, 425-437 (1984).

73. H. Nikjoo, M. Terrissol, R. N. Hamm, J. E. Turner, S. Uehara, H. G. Paretzke and D. T. Goodhead, Comparison of energy deposition in small cylindrical volumes by electrons generated by Monte Carlo track structure codes for gaseous and liquid water. *Radiat. Prot. Dosim.* **52**, 165-169 (1994).

74. H. Nikjoo and S. Uehara, Comparison of various Monte Carlo track structure codes for energetic electrons in gaseous and liquid water. In *Computational Approaches in Molecular Radiation Biology. Monte Carlo Methods* (M. N. Varma and A. Chatterjee, Eds.), pp. 167-185. Plenum Press, New York, 1994.

75. R. S. Caswell and S. M. Seltzer, Monte Carlo and analytic methods in the transport of electrons, neutrons, and alpha particles. In *Computational Approaches in Molecular Radiation Biology. Monte Carlo Methods* (M. N. Varma and A. Chatterjee, Eds.), pp. 115-136. Plenum Press, New York, 1994.

76. NCRP, *Biological effects and exposure limits for "hot particles"*. Report 130, p. 22, National Council on Radiation Protection and Measurements, Bethesda, MD, 1999.

77. M. J. Berger, S. M. Seltzer, R. Wang and A. Schechter, *Elastic Scattering of Electrons and Positrons by Atoms: Database ELAST.* Report NISTIR 5188, U.S. Department of Commerce, Gaithersburg, MD, 1993.

78. M. E. Riley, *Relativistic, elastic electron scattering from atoms at energies greater than 1 keV*, Report No. SLA-74-0107, Sandia Laboratories (1974).

79. M. E. Riley, C. J. MacCallum and F. Biggs, Theoretical electron-atom elastic scattering cross sections. Selected elements, 1 keV to 256 keV. *At. Data Nucl. Data Tables* **15**, 443-476 (1975).

80. J. B. Mann, SCF Hartree-Fock results for elements with two open shells and for the elements francium to nobelium. *At. Data Nucl. Data Tables* **12**, 1-86 (1973).

81. J. B. Mann and J. T. Waber, Self-consistent relativistic Dirac-Hartree-Fock calculations of lanthanide atoms. *At. Data* **5**, 201-229 (1973).

82. J. P. Desclaux, A multiconfiguration relativistic Dirak-Fock program. *Comp. Phys. Comm.* **9**, 31-45 (1975).

83. S. M. Seltzer, Electron-photon Monte Carlo calculations: the ETRAN code. *Appl. Radiat. Isot.* **42**, 917-941 (1991).

84. ICRU, *Stopping powers for electrons and positrons.* Report 37, International Commission on Radiation Units and Measurements, Bethesda, MD, 1984.

APPENDIX

NOREC, a Monte Carlo electron track-structure code for liquid water

The Monte Carlo code OREC was developed to transport primary electrons and their secondaries in liquid water. We describe here several recent modifications to update and revise the code, which we have renamed NOREC.

The original versions of OREC (*46, 47*) employed electron differential elastic cross sections for liquid water derived from phase-shift calculations for energies up to 1 keV and from first Born approximation calculations at higher energies. Scattering from hydrogen and oxygen atoms was treated incoherently and largely non-relativistically. Later versions (*48*) used phase-shift values up to 10 keV and Thomas-Fermi model computations at higher energies. It was recognized by the developers of OREC that the elastic-scattering model was crude and warranted further study. Over time, it became apparent that OREC generally underestimated the deep penetration of electrons when compared with the work of other investigators. This shortcoming was attributed to possible deficiencies in the elastic-scattering cross sections (*75, 76*). An attempt was made to correct this problem in one particular application of OREC (*64*), but further work was needed. This state of affairs was a principal factor that led us to look critically not only at the elastic scattering, but also at various other components in OREC, some of which date back to its origins.

The new code employs the database, ELAST, developed at the National Institute of Standards and Technology (NIST) for the differential cross sections for the elastic scattering of electrons by atoms (*77*). The NIST cross sections are provided for electron energies between 1 keV and 1 MeV. The cross sections in ELAST were calculated by using the computer code originally developed by Riley (*78*). The relativistic partial-wave computations treat elastic scattering from a static, screened Coulomb potential. Phase shifts are obtained through numerical solution of the Dirac equation with use of the WKB approximation. Later work by Riley *et al.* (*79*) utilized electron density distributions from Mann (*80*) and Hartree-Fock wave functions from Mann and Waber (*81*). The NIST work uses the later version of Riley's code (*79*) and the electron density distributions based on wave functions obtained with the code of Desclaux (*82*). The ELAST database extends the earlier compilations in a number of ways (e.g., higher energies, finer angular grid, and applications to positrons). It has been used to compute electron back scattering, electron and positron multiple scattering, and to refine the ETRAN code (*83*). Incorporation of the ELAST database for H and O into NOREC represents a major improvement from the relatively crude treatment of elastic scattering in OREC. In addition to the revision of the numerical values themselves, a much finer grid is now used in NOREC to represent the small-angle scattering in the forward direction.

Below 1 keV, the earlier OREC elastic angular distributions have been smoothly merged with the NIST data. Hartree-Fock wave functions were used to calculate charge-density distributions for H and O atoms. Integrals over these distributions were then

employed to construct the potential functions for the partial-wave analyses and the computation of phase shifts for the scattering.

The total elastic inverse mean free paths employed in NOREC, are shown in Fig. 26, where they are compared with the old data of OREC. The mean free paths between elastic collisions are substantially larger in NOREC. Because of the tortuous nature of electron tracks, differences between the two versions of the code become more pronounced at higher energies.

The original motivation for the revisions described here was the insufficient degree of deep penetration of energetic electrons. Specifically, depth-dose distributions for 800-keV electrons normally incident on a semi-infinite slab of water, calculated with OREC and with the condensed-history Monte Carlo code ETRAN (*83*), showed poor agreement [see Fig. 3 in (*75*)]. The OREC model was found to yield significantly less penetrating electron tracks at such high energies. When the elastic-scattering cross sections in OREC were replaced with the NIST values, better agreement with ETRAN was found. The remaining discrepancy, however, was unacceptably large. Attention was shifted to examining other aspects of OREC, particularly the angular distributions for ionizing collisions. It was discovered that one step in this part of the code was entered in non-relativistic form. Although it was adequate at low energies, it was inappropriate at high energies. Presumably, this circumstance dates back to the earliest days in the development of OREC, when the highest energies considered were 10 keV (*46*) and 100 keV (*47*). The replacement of this step with the proper formula in NOREC brought the calculated depth-dose distribution for 800-keV electrons into good agreement with

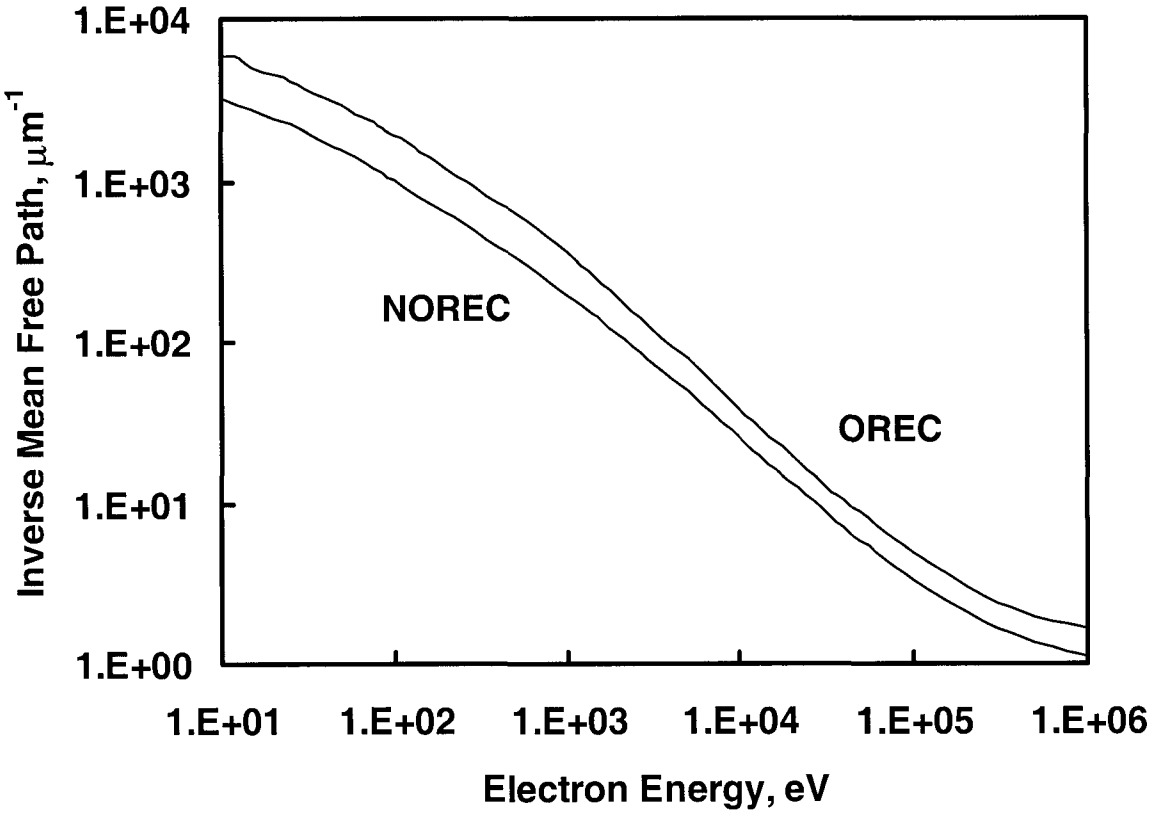

Figure 26. Total elastic inverse mean free paths, or macroscopic cross sections, in OREC and NOREC.

ETRAN, as shown in Fig. 27. The result of changing only the elastic scattering in OREC is also displayed.

Calculations of depth-dose distributions for parallel beams of monoenergetic electrons normally incident on a slab of liquid water, similar to those of Turner *et al.* (*63*), were performed by using both OREC and NOREC for selected energies between 50 keV and 1 MeV. The calculated average pathlength as a function of the initial energy, shown by the top two curves in Fig. 28, is the same for both codes since pathlength is not affected by changes in the elastic scattering or angular distributions following ionizing collisions. The middle two curves show the average value of the maximum depth reached by an electron. The increased penetration of energetic electrons in NOREC, compared with OREC, is significant. This change is demonstrated further in the bottom two curves, which give the depth at which the maximum dose occurs for monoenergetic electrons. Although there is a clear increase in penetration for electron tracks generated by NOREC above ~300 keV, the modifications made to revise OREC have little or no effect on results of the current study.

Like its predecessor, NOREC calculates the detailed event-by-event transport of a primary electron and all of its secondaries in liquid water over a range of energies from 1 MeV to below 7.4 eV, the threshold assumed for electronic transitions in liquid water. NOREC was implemented as a C++ class that can be conveniently embedded into application drivers that require electron tracks.

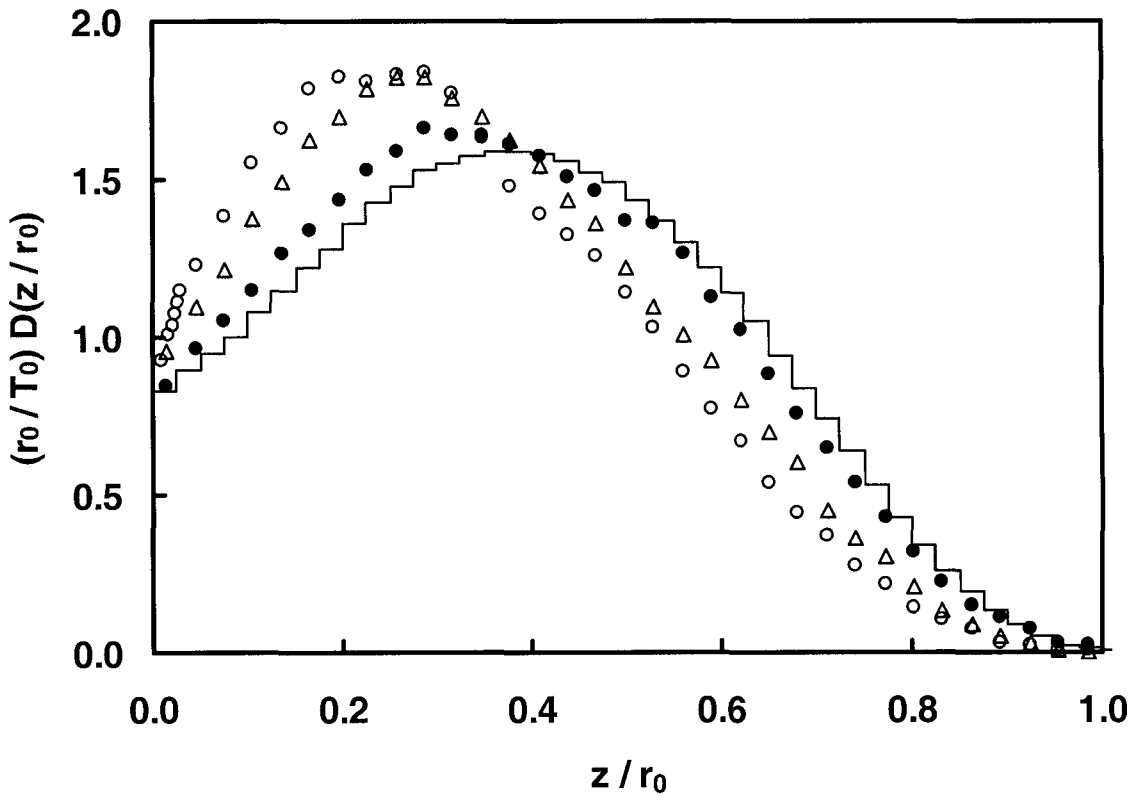

Figure 27. Depth-dose distribution for a parallel beam of electrons with an initial energy, T_0, of 800 keV normally incident upon a slab of water. The depth, z, is expressed in units of the CSDA range, r_0 (*84*). The histogram shows the result from calculations with ETRAN (*83*). The open circles are obtained from OREC. The triangles show the results obtained from OREC with only the elastic cross sections revised. The closed circles are the final results calculated with NOREC. Dose is expressed in units of $keV \cdot \mu m^{-1}$ and then scaled by $(r_0 \cdot T_0^{-1})$ to yield a dimensionless quantity. The areas under each curve are identical.

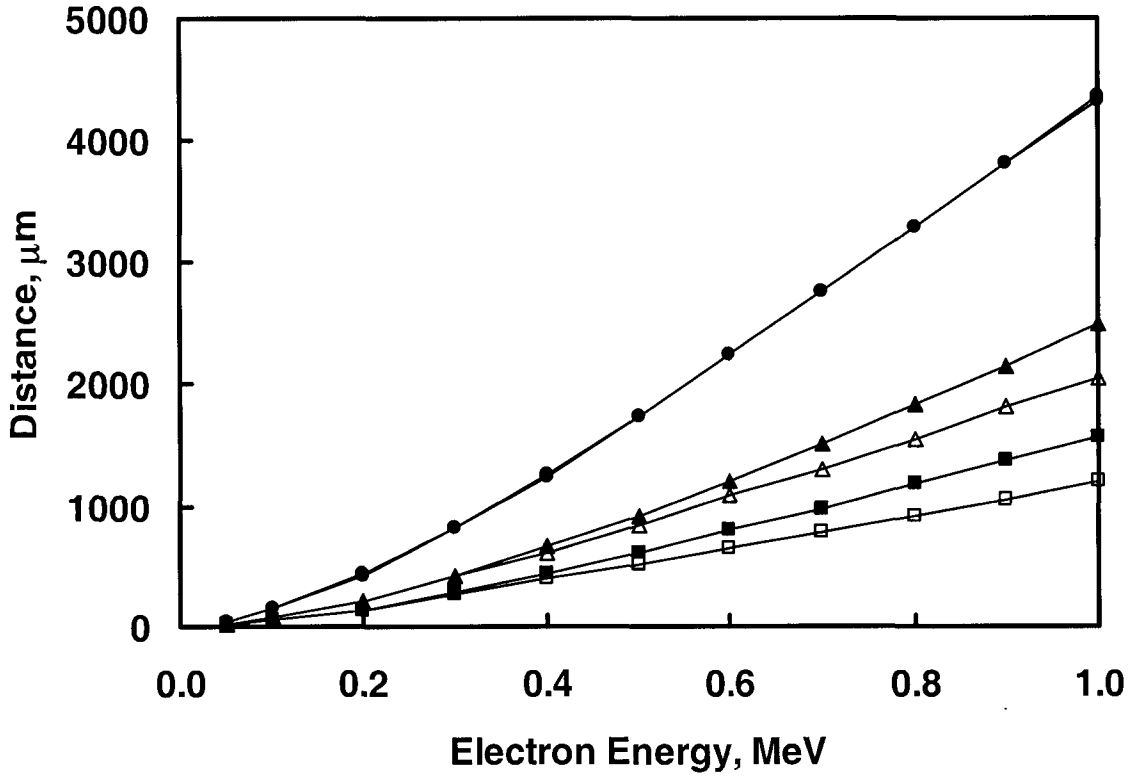

Figure 28. Penetration capability of electrons in water: average pathlength (circles), average penetration depth (triangles), and depth of maximum dose (squares). Open symbols – OREC, closed symbols – NOREC.